THESIS

AIRBORNE RADAR QUALITY CONTROL AND ANALYSIS OF THE RAPID INTENSIFICATION OF HURRICANE MICHAEL (2018)

Submitted by

Alexander J. DesRosiers

Department of Atmospheric Science

In partial fulfillment of the requirements

For the Degree of Master of Science

Colorado State University

Fort Collins, Colorado

Fall 2020

Master's Committee:

Advisor: Michael M. Bell

Elizabeth Barnes
Suren Chen

ABSTRACT

AIRBORNE RADAR QUALITY CONTROL AND ANALYSIS OF THE RAPID INTENSIFICATION OF HURRICANE MICHAEL (2018)

Improvements made by the National Hurricane Center (NHC) in track forecasts have outpaced advances in intensity forecasting. Rapid intensification (RI), an increase of at least 30 knots in the maximum sustained winds of a tropical cyclone (TC) in a 24 hour period, is poorly understood and provides a considerable hurdle to intensity forecasting. RI depends on internal processes which require detailed inner core information to better understand. Close range measurements of TCs from aircraft reconnaissance with tail Doppler radar (TDR) allow for the retrieval of the kinematic state of the inner core. Fourteen consecutive passes were flown through Hurricane Michael (2018) as it underwent RI on its way to landfall at category 5 intensity. The TDR data collected offered an exceptional opportunity to diagnose mechanisms that contributed to RI.

Quality Control (QC) is required to remove radar gates originating from non meteorological sources which can impair dual-Doppler wind synthesis techniques. Automation of the time-consuming manual QC process was needed to utilize all TDR data collected in Hurricane Michael in a timely manner. The machine learning (ML) random forest technique was employed to create a generalized QC method for TDR data collected in convective environments. The complex decision making ability of ML offered an advantage over past approaches. A dataset of radar scans from a tornadic supercell, bow echo, and mature and developing TCs collected by the Electra Doppler Radar (ELDORA) containing approximately 87.9 million radar gates was mined for predictors. Previous manual QC performed on the data was used to classify each data point as weather or non-weather. This varied dataset was used to train a model which classified over 99% of the radar gates in the withheld testing data succesfully. Creation of a dual-Doppler analysis from a tropical depression using ML efforts that was comparable to manual QC confirmed the utility of this new method. The framework developed was capable of performing QC on the majority of the TDR data from Hurricane Michael.

Analyses of the inner core of Hurricane Michael were used to document inner core changes throughout RI. Angular momentum surfaces moved radially inward and became more vertically aligned over

time. The hurricane force wind field expanded radially outward and increased in depth. Intensification of the storm became predominantly axisymmetric as RI progressed. TDR-derived winds are used to infer upper-level processes that influenced RI at the surface. Tilting of ambient horizontal vorticity, created by the decay of tangential winds aloft, by the axisymmetric updraft created a positive vorticity tendency atop the existing vorticity tower. A vorticity budget helped demonstrate how the axisymmetric vorticity tower built both upward and outward in the sloped eyewall. A retrieval of the radial gradient of density temperature provided evidence for an increasing warm core temperature perturbation in the eye. Growth of the warm core temperature perturbation in upper levels aided by subsidence helped lower the minimum sea level pressure which correlated with intensification of the near-surface wind field.

ACKNOWLEDGMENTS

The research presented here was made possible through the support of many who have helped propel me forward on this path. I am grateful for the guidance, knowledge, and assistance provided by my advisor Michael M. Bell. The latitude Michael allowed in the pursuit of these projects has transformed me into a competent researcher capable of independent thought and inquiry in the field which interests me most. I appreciate the insight and support provided by my other committee members, Elizabeth Barnes and Suren Chen, as I prepared this thesis. I thank Bruno Melli, a former software engineer in the Bell research group, for efforts which provided initial direction and structure to the machine learning airborne radar quality control framework. The manual quality control efforts of Wen-Chau Lee, Huaqing Cai, Hannah Murphey, and Michael Bell populated an invaluable training dataset for the machine learning model. We would like to acknowledge operational, technical and scientific support provided by NCAR's Earth Observing Laboratory, sponsored by the National Science Foundation. Data sets obtained in Hurricane Michael were provided by the NOAA Hurricane research Division (HRD) of AOML. I cherish the helpful comments, assistance with coding, overall support, and understanding of the entire Bell research group. Furthermore, I am thankful for the faculty, staff, and students of the Colorado State University Department of Atmospheric Science who all participate in the creation and maintenance of a welcoming academic community which fosters intellectual growth so well.

I am indebted to my mother, Denise DesRosiers, who handled a tumultuous situation to not only provide me the freedom to complete this work, but also encouraged me along the way. The support of my girlfriend Devon, brother Michael, and sister Mary was instrumental. Research opportunities during my time as an undergraduate helped prepare me for graduate level work. I appreciate the Colorado State Research Experience for Undergraduates (REU) program, NOAA Aircraft Operations Center, and Corene Matyas for facilitating these. I am thankful for the funding and opportunities provided by the American Meteorological Society and Lockheed Martin through the AMS Graduate Fellowship. This research was also supported by National Science Foundation awards AGS-1701225 and OAC-1661663, Office of Naval Research awards N000141613033 and N000142012069, and National Oceanic and Atmospheric Administration award NA19OAR4590245.

DEDICATION

To my father: James DesRosiers

Your love, support, and unrelenting smile in the face of unthinkable circumstance continue to and always will inspire.

TABLE OF CONTENTS

LIST OF TABLES

LIST OF FIGURES

CHAPTER 1

INTRODUCTION

1.1 MOTIVATION

The United States (US) is no stranger to hurricane impacts. These storms bring life threatening weather conditions and leave a wake of costly destruction with regularity. From 1900 to 2017, there were 206 recorded hurricane landfalls in the mainland US. The price tag from the total count sits at approximately $2 trillion in normalized damage. When averaged over the period, each year adds an additional $17 billion of damage to the total (Weinkle et al. 2018). The past 3 Atlantic hurricane seasons and the current have been particularly destructive due in part to a weather phenomenon known as rapid intensification (RI). The National Hurricane Center (NHC) defines RI as an increase in the maximum sustained winds of a tropical cyclone (TC) of at least 30 knots in a 24-hour period. From 2017 through present, 7 landfalling hurricanes which underwent a period of RI at some point during their life cycle and attained major hurricane status have struck the US.

Harvey (2017), Irma (2017), Maria (2017), Florence (2018), Michael (2018), Dorian (2019), and now Laura (2020) make up the list of recent storms which live in infamy after eventful US landfalls. Of these listed storms, Dorian and Florence were the only two not classified as major, category 3 or above, hurricanes on the Saffir Simpson Hurricane Wind Scale at the time of US landfall. However, the rapid deepening of the vortices during RI made them more formidable systems than the intensity the maximum sustained wind at landfall implied. An investigation of the metrics by which we classify hurricane intensity found pressure to be a greater predictor of damage than maximum wind speed (Klotzbach et al. 2020). The study proposed a revised hurricane intensity scale focused on pressure which better characterizes the overall strength of the vortex than a wind measurement. On the revised scale, the 956 hPa minimum sea level pressure reported by NHC Best Tracks at landfall for both Florence and Dorian would elevate them to category 3 status. With a lower maximum wind than expected in a major hurricane, but a pressure indicative of one, a larger wind field resulted from the pressure gradient. Increased wind field size allows for higher volumes of water to be pushed ashore as well as a larger footprint of wind damage in the affected region. When considering the revised pressure scale, the number of landfalling major hurricanes rises from 5 to 7 over the last four years. An improved understanding of the process which allowed these storms to become so destructive requires continued research.

The sudden changes in intensity have proven challenging for forecasters (DeMaria et al. 2014; Trabing and Bell 2020). The environmental conditions which allow RI are well known, but RI is likely controlled by internal dynamical processes present in addition to a favorable environment (Hendricks et al. 2010). Observations taken inside storms undergoing RI are needed to give a close up look at these internal processes which must be better understood to forecast these events with accuracy.

1.2 Aircraft Reconnaissance and Airborne Radar

The NOAA Hurricane Hunters provide both real time information to support forecasters and data for later use by TC researchers. The NOAA WP-3D Orion Hurricane Hunter aircraft (P3) offers the ability to fly through a TC with instruments on board to document the structure and environment inside the storm. The P3 is equipped with a tail Doppler radar (TDR) which allows for retrieval of the storm's 3-dimensional wind field. The fore/aft scanning technique alternates the radar between scans in each direction to produce the pseudo-dual-Doppler measurements necessary to retrieve a wind field (Jorgensen et al. 1996). Accurate winds can only be determined if adequate quality control (QC) is performed on the data. Radar echoes can originate from non-weather sources. Non-meteorological radar data must be removed from the Doppler velocity field to prevent errors in retrieved weather-related velocities. QC of radar data is a time intensive process when performed manually. Previous efforts to automate this process have used rules-based approaches that apply thresholds which may both include non-weather data and exclude weather data depending on the thresholds used (Bell et al. 2013; Gamache et al. 2008). An improved automation of QC must be capable of complex decision making to improve beyond basic thresholding.

A machine learning (ML) random forest technique was employed to create a generalized QC method for airborne radar data in convective environments. Observations from the Electra Doppler Radar (ELDORA) that were manually QCed by different researchers were used to train the model with data from mature and developing tropical cyclones, a tornadic supercell, and a bow echo. The ELDORA dataset presented the opportunity to not only automate QC for the explicit purpose of Hurricane Hunter data, but to extend this method to TDR data collected in a wide range of atmospheric phenomenon. Successful QC of the ELDORA dataset is encouraging but ELDORA is capable of easily and accurately capturing most extreme velocity data without being subject to folding.

The current TDR aboard the P3 has a maximum unambiguously detectable radial velocity below the wind speeds found in strong hurricanes. When observed velocities fall outside the detection range,

the scale crosses over to the opposite maximum value and reports the value incorrectly. Correcting these folding errors requires adding or subtracting the correct number of Nyquist intervals ($2V_{max}$) to the radial-velocity data obtained from the radar (Houze Jr. et al. 1989). Correctly guessing the number of intervals is easier for automated techniques developed for this task (Bargen and Brown 1980) when non-meteorological clutter is not present. Velocity folding provides an added challenge to the QC of Hurricane Hunter data. The random forest model was also tested as a suitable QC method for the Hurricane Michael data. Promising results from the ML technique in both datasets provide promise for the technique to be generalized to multiple radar platforms and convective environments.

1.3 Rapid Intensification of Hurricane Michael

The detailed analysis of a TC inner core that TDR data affords has contributed to a great deal of progress in understanding of internal processes affecting intensity. The roles eyewall replacement cycles (Houze Jr. et al. 2007), convective bursts near the storm center (Rogers et al. 2013), and potential vorticity structure in the eyewall (Martinez et al. 2019) play in modulating intensity have greater clarity due to TDR data. Hurricane Michael offered an excellent opportunity to further examine inner core processes during an RI event resulting in the fourth recorded landfall of a category 5 hurricane in the US. The storm was well sampled by the TDR aboard the P3 as it strengthened on a northward track through the Gulf of Mexico towards the Florida panhandle. RI began and proceeded regardless of the presence moderate vertical wind shear (Beven et al. 2019). Despite the less than ideal environment, internal processes were able to overcome the shear allowing Hurricane Michael to still undergo RI.

The cooperation between cloud-scale moist convection and cyclone-scale circulation during TC intensification and maintenance is long standing knowledge (Ooyama 1969). More current studies of intensification and RI have focused on the finer cloud-scale. Intense convective towers with anomalous updraft speeds in the inner core which enhance the circulation locally have been correlated with intensification and the onset of RI (Van Sang et al. 2008; Rogers et al. 2013). However, these discrete convective elements eventually give way to vertical mass flux being accomplished by more efficient axisymmetric vertical motion with increasing vertical extent (Rogers 2010; Nolan et al. 2007). Upper level processes have also been a focus in RI literature with warming in the upper levels of the eye being a recurring theme in simulations of deep and intense TCs (Chen and Zhang 2013; Stern and Zhang 2010; Stern and Nolan 2012). Warming in the upper levels of the troposphere can result in pressure falls at the surface below it (Hirschberg and Fritsch 1993) which would result in increasing near surface

winds. Observations have been leveraged to learn more about vertical structure in TCs, but questions remained about upper level dynamics where past data has been sparse (Stern and Nolan 2009).

Multiple aircraft reconnaissance missions during RI in Hurricane Michael allowed for detailed observation of the upper levels. Data from each of the 14 passes through the storm were input into the three dimensional variational technique SAMURAI which yields a snapshot of the kinematic fields in the storm. Analyses of the storm were used in a vorticity focused framework to piece together the mechanisms responsible for building the eyewall vorticity tower into the upper levels when axisymmetric budget terms were more dominant. Well-defined axisymmetric structure and upper level processes were investigated in regards to enhancing RI of the near surface wind during RI.

1.4 Research Objectives

The main purpose of this thesis is to further physical understanding of RI. To accomplish this goal, a comprehensive TDR dataset from Hurricane Michael was utilized. An innovative approach to the airborne radar QC problem was required to automate the time-consuming manual steps and make more time for analysis. To meet these ends, the following research objectives were pursued:

(1) Improve airborne radar data QC by automation with ML

(2) Document evolution of the inner core of Hurricane Michael during RI

(3) Explain the growth of the vorticity tower vertically and its impact on RI of the wind field

Chapter 2 presents a random forest ML model trained to QC airborne radar data from a variety of convective phenomenon. Chapter 3 examines the RI of Hurricane Michael in the Gulf of Mexico and infers upper level processes that contributed to the process. Chapter 4 is a summation of the findings of research presented in this thesis as well as recommendations for future work.

CHAPTER 2

AIRBORNE RADAR QUALITY CONTROL WITH MACHINE LEARNING

2.1 INTRODUCTION

Airborne Doppler radar has a rich history of advancing knowledge in the meteorology community through close range data collection during intensive observations. Despite the utility provided by airborne Doppler radar, the analysis process comes with challenges unique to the platform. For accurate wind synthesis to take place, motion of the plane carrying the radar must be removed to establish Earth relative locations of data points (Lee et al. 2003). Efforts to correct the problem of motion for data users began with navigation corrections to remove errors in the inertial navigation system (Testud et al. 1995) and continue to be improved on (Cai et al. 2018). Although strides have been made on the platform motion issue, the barrier of painstaking and time consuming quality control (QC) of the data remains for those who seek high quality analyses for research.

A full automation of airborne radar QC was developed for tail Doppler radar (TDR) to analyze Hurricane Hunter Data in real time (Gamache et al. 2008). A considerable reduction in the amount of effort required in the QC process was provided by an algorithm (Bell et al. 2013) developed for use in SOLO II radar editing software from the National Center for Atmospheric Research (NCAR) (Oye et al. 1995). The effort brought automated QC to an interactive platform that allows further user input if more thorough QC is required. By using a rules-based approach that sets thresholds for data retention, both of the aforementioned techniques suffer from a trade-off between how much 'good' weather data is retained versus how much 'bad' non-weather data is removed. If the thresholds are increased then nearly all non-weather data can be removed, but valuable weather data is discarded with it. Similarly, lower thresholds allow more retention of good data, but a greater quantity of bad data that must be removed manually by a trained expert remains. Thus, for a QC process to be done without manual intervention, strict thresholds must be applied bringing with it the unintentional removal of large quantities of valuable weather data. An improved QC algorithm requires more complex decision making than the more rigid thresholding of rules-based approaches utilized in past techniques.

Among the distinguished history of airborne Doppler radars, the Electra Doppler Radar (ELDORA) (Hildebrand et al. 1996) operated by NCAR enabled numerous advances in knowledge in a variety of

areas. The radar was utilized in several field campaigns investigating different convective phenomena including both mature (Hence and Houze 2008) and developing tropical cyclones (Bell and Montgomery 2010), tornadoes (Wakimoto and Liu 1996), and bow echoes (Wakimoto et al. 2006). The field campaigns which gathered this data were the Hurricane Rainband and Intensity Change Experiment (RAINEX), Tropical Cyclone Structure (T-PARC/TCS08), Verification of the Origins of Rotation in Tornadoes Experiment (VORTEX), and Bow Echo and Mesoscale Convective Vortex Experiment (BAMEX). The radar data from each of these cases is composed of approximately 87.9 million radar pixels, also known as radar gates. The diverse dataset collected by ELDORA and QCed by researchers make it a prime candidate for developing an improved QC method for airborne Doppler radar data in convective environments.

In order to provide the complex decision making capability an improved algorithm requires, a machine learning (ML) approach has been employed. ML methods have been applied to a range of tasks including cancer detection, stock market analysis, and even the automatic composition of music. The advantages of ML are currently being realized in the field of meteorology with opportunities to advance remote sensing retrievals, data assimilation, model physics calculation, forecasting, and data QC (Boukabara et al. 2019). The recent successful implementation of ML into a QC algorithm for ground based radar (Lakshmanan et al. 2014) further motivated an attempt with airborne Doppler radar. A relatively straightforward ML technique, the random forest (Louppe 2014), creates an array of decision trees which can be used to classify each radar gate individually. The capabilities of ML were used to improve on the current state of QC algorithms for the purpose of producing a research quality dual-Doppler wind synthesis from TDR data with minimal effort.

2.2 Methodology

Training and testing of the random forest model utilized the same data set from Bell et al. (2013) which consists of TDR data collected by ELDORA during the RAINEX, TPARC/TCS08, BAMEX, and VORTEX field experiments. The variety of airborne data collected is intended to showcase the ability of this method to succeed in a variety of convective environments. All data used in training was QCed via a combination of automated and manual techniques by a radar expert, providing an extensive training dataset from many months of dedicated effort. The previous QC provided the information required for training a machine learning model to recreate these past manual QC efforts with greater speed and minimal user input.

2.2.1 Model Training and Testing

A flowchart of the method, shown in Fig. 2.1a, is a useful visual aid for following the technique. Data for the model mined from the ELDORA data set contained the radar range, moments (radar reflectivity in dBZ, Doppler velocity in m s^{-1}, and normalized coherent power), and the derived mathematical quantities of average and standard deviation for each of these moments relative to neighboring radar gates. Normalized coherent power (NCP) is a measure of the quality of a radar observation ranging from 0 to 1 where 1 is likely high quality data. NCP evaluates quality by checking how consistent radar phase shifts are from one sample to the next. Other properties such as the isolation of a radar gate, probability of a radar gate being affected by the ground, and range normalized through division by aircraft altitude were also calculated and provided to the model as predictors. The isolation parameter calculates the ratio of neighboring radar gates reporting values to total neighboring gates in a square area centered on the gate in question. The probability of a ground gate was adapted from geometric radar beam considerations discussed in Testud et al. (1995) which aims to identify radar echoes due to the ground. Each radar gate in the dataset includes all 14 predictors described which are listed in Fig. 2.2. Radar gates in ELDORA scans which did not report any data were excluded from the dataset as they can automatically be left blank during implementation. The mined predictors make up the 'X' array which is used to classify data as weather or non-weather. The classification made by a human radar expert was stored in the 'Y' array which is a binary for each radar gate where a class of 1 was assigned to weather echoes and 0 to non-weather data. Comparison of the original scan which only received navigation corrections to the post manual QC edited fields of the scans used for analysis determined the classification of a radar gate as weather or non-weather.

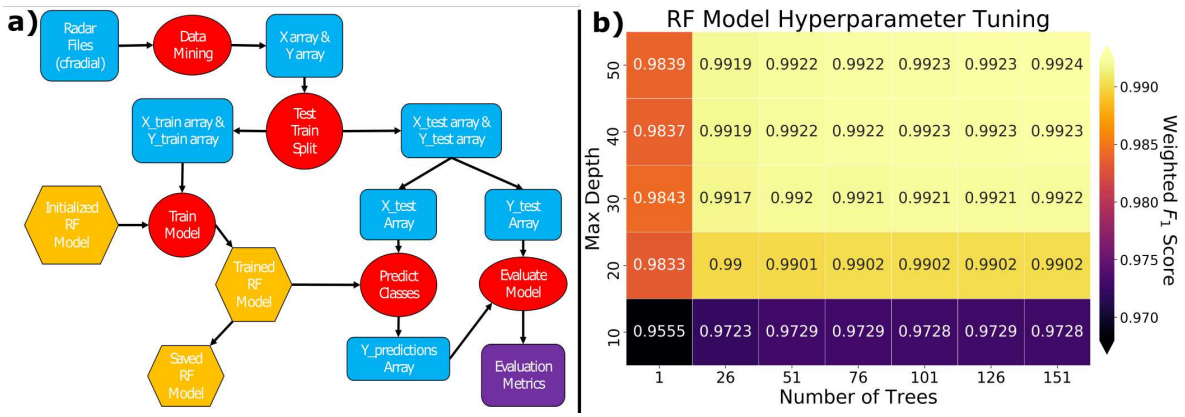

FIG. 2.1. a) A flow chart describing the process with which a random forest model was trained, tested, and evaluated with mined radar data to learn the QC process. b) A heatmap depicting F_1 score performance of each hyperparameter combination tested. Colors and values in each square indicate model performance for each combination of hyperparameters. Axes are the number of trees and depth to which decisions can be made in each model.

An initialized model, the specifications of which are discussed in the next section, was trained with the mined data from the ELDORA dataset. The X and Y arrays from the data collection stage were split at random with 80% and 20% reserved for training and testing respectively. Initial splitting of the data before training ensures the model has not previously encountered the testing set. The trained model classified all radar gates in the X testing array to create a new set of classifications. Predicted classes were compared to the true classifications in the Y testing array. Evaluation metrics were produced to assess how well the model retained and removed weather and non-weather echoes.

2.2.2 Hyperparameter Tuning

Training and testing of the model was performed with Python's SciKit-Learn library (Pedregosa et al. 2011). Hyperparameters, which are set to control the learning process, are very important to maximized model performance. Choice of hyperparameters for a model determines its complexity. A model that is too complex is prone to overfitting to the training set at the expense of performance on unseen data. A model that is too simple fails to capture important characteristics of the data and underperforms on the classification task (Claesen and De Moor 2015). Tuning of the model was focused on varying two hyperparameters, the number of trees and the maximum depth of a tree. Adjusting the number of trees simply changes the count of decision trees in the random forest. Maximum depth assigns a limit to how far the trees can branch downward further sorting the data into classes. Testing the impacts of hyperparameters on model performance helps ensure the appropriate level of model complexity is achieved.

There is an unequal distribution of classes between weather and non-weather radar gates in the ELDORA dataset. To combat the inequality, class weights used in training were balanced by making the weights of the classes inversely proportional to class frequencies in the data. The adjusted weights assigned greater importance in model training to the less common class of weather data. As a consequence of imbalance, accuracy is not an effective metric with which to assess the performance of the model's binary classification. For example, a model that always classifies radar gates as the most common class would receive a deceivingly good accuracy score in a data set consisting mainly of that class, regardless of the model being unable to perform classification. The F_1 score was substituted for accuracy as the evaluation metric. The definitions of these quantities are as follows with abbreviations used for true positives (TP), true negatives (TN), false positives (FP), and false negatives (FN):

$$Precision = \frac{TP}{TP+FP} \ , \ Recall = \frac{TP}{TP+FN} \ , \ F_1 Score = \frac{2*Precision*Recall}{Precision+Recall} \tag{2.1}$$

When evaluating these equations for each class of data, a positive is a guess that the data belongs to the class in question while a negative is the opposite. True or false denotes the correctness of the model guess. Precision is a ratio of correctly predicted positive observations to the total count predictions for positive including those which were false. Recall is the ratio of correctly predicted positives to the total count of positives in the training set. F_1 score was calculated for each class of data and accounts for both precision and recall.

To further address class imbalance in the data, a weighted F_1 score was calculated to assess each model during tuning. The weighting takes the F_1 score for weather and non-weather data classes and averages them based on the balanced class weights calculated during model training. The GridSearchCV functionality from SciKit-Learn was employed for iterative training and testing of random forest models with different combinations of the two varied hyperparameters. The aim was to find which model exhibits a high weighted F_1 score while not unnecessarily increasing complexity to a point of diminishing return. To further prevent overfitting, a cross validation scheme was included in the search. Before each model is tested, the full data set was shuffled, and split into the default count of five stratified groups, or folds, with class distributions similar to the full set. For each combination of hyperparameters, a model was trained on four folds leaving the remaining one for testing. This step was repeated until each fold had been used for testing and five models were trained and scored. The weighted F_1 score given for each combination of hyperparameters is an average of scores from the 5 different models created with those specifications. Due to the computing cost of the exhaustive method,

only one minute of radar data from each phenomenon in the ELDORA data set was used for tuning. Results of the hyperparameter tuning (Fig. 2.1b), show that past a certain level of model complexity, there is not much performance to be gained. After the weighted F_1 score of 0.992 is achieved, most increases in score are minuscule. The hyperparameter combination of 51 trees with a maximum depth of 30 which first achieved the score of 0.992 was chosen to train a more thorough model with the full dataset.

2.3 Results

	Predicted Non-weather	Predicted Weather
Non-weather	10474021 (99.2%)	83854 (0.8%)
Weather	55161 (0.8%)	6972281 (99.2%)

Feature Importance of Model Predictors			
Predictor Name	Rank & Score	Predictor Name	Rank & Score
NCP	1) 0.2216	Altitude	8) 0.048
SD of Velocity	2) 0.1698	SD of NCP	9) 0.045
Avg. of NCP	3) 0.1297	Avg. of Reflectivity	10) 0.0429
Prob. of Ground Gates	4) 0.0802	Range	11) 0.0302
Reflectivity	5) 0.0597	Isolation	12) 0.0298
SD of Reflectivity	6) 0.0595	Velocity	13) 0.0231
Normalized Range	7) 0.0496	Avg. of Velocity	14) 0.011

FIG. 2.2. Confusion matrix outlining model performance on the testing set. Predictors used by the model are ranked based on feature importance which indicates ability of a predictor at classifying data points early and effectively. SD indicates the standard deviation of a quantity and Avg. is an average with both calculated with respect to neighboring points.

The full ELDORA training dataset consists of airborne radar data from VORTEX, BAMEX, RAINEX, and TPARC/TCS08 collected over the course of 6, 11, 22, and 9 minutes respectively. Following the steps outlined in the flowchart (Fig. 2.1a), a generalized model for radar QC was trained and evaluated. Model performance metrics and information are outlined in Fig. 2.2. The accuracy and weighted F_1 score are both 0.992, in good agreement with the confusion matrix which reports retention of weather data and removal of non-weather data at a 99.2% success rate in the testing set. Impurity-based feature importance for random forest predictor variables which were obtained through the SciKit-Learn library are ranked based on the predictors that affect the most samples and split data most effectively

(McGovern et al. 2019). For a predictor to receive a high feature importance relative to others, it should be used higher up in the tree to divide data and be effective at decreasing impurity in the groups the predictor splits the data into. The rankings demonstrate the utility of taking the mathematical quantities of average and standard deviation which relate a radar gate to its surrounding and aid in determining its likelihood of being weather data. The high ranking of custom predictors created for the model such as normalized range and probability of ground gates show the utility of considering spatial context information during radar QC.

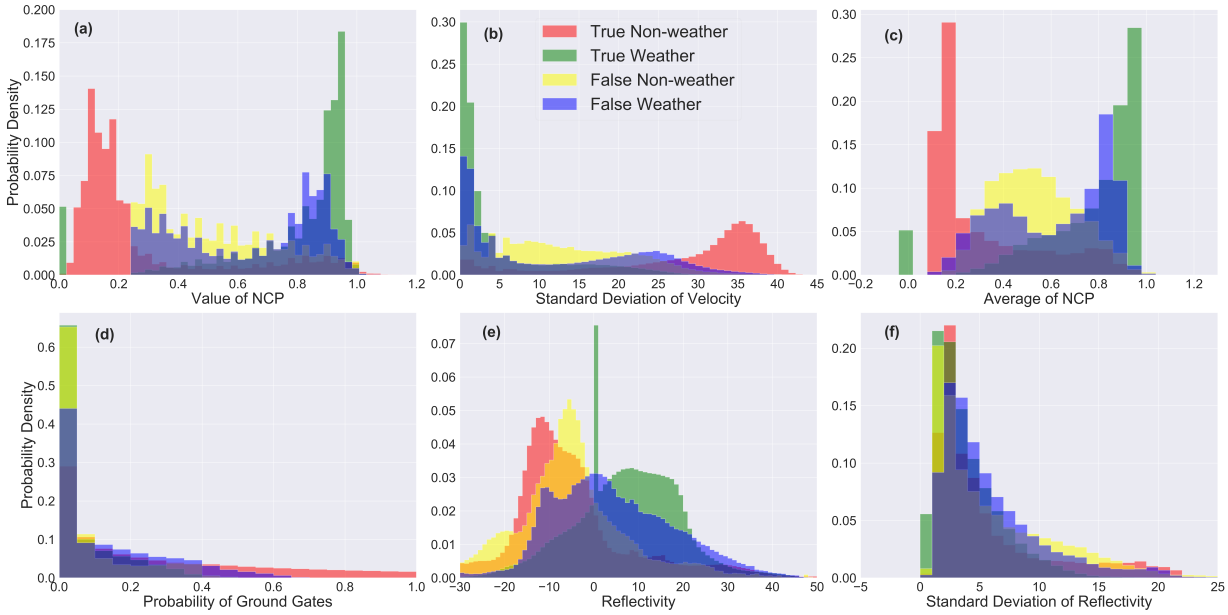

FIG. 2.3. A probability density function (PDF) was calculated for each of the top 6 predictors (normalized coherent power (NCP) (a), SD of Velocity (b), Avg. of NCP (c), Prob. of Ground Gates (d), Reflectivity (e), and SD of Reflectivity (f)) classified by both what the model predicted and if that prediction was correct. The x axis indicates value of the predictor and the y axis displays PDF values which sum to 1. The analysis is composed of data from the RAINEX field campaign not previously seen by the model in the training or testing sets.

A telling test of the model to evaluate its suitability for airborne radar QC is to use it with data not included in the ELDORA dataset used with the model up to this point. During the RAINEX field campaign on 6 September 2005, ELDORA was used to observe intense convective activity on the southern edge of the tropical depression which later became Hurricane Ophelia (Houze et al. 2009). TDR data collected by ELDORA during a close-up 15 minute fly-by leg of the convective feature was cleaned with the machine learning QC model for comparison with the original manual QC carried out for analysis of this feature. Comparison of the ML and manual QC methods showed a decrease in performance from the statistics achieved with the prior withheld testing set. Bad data was removed at a 95.6% rate while

98% of good data was retained. The decrease of these rates compared to previous tests can initially be attributed to two factors. The Ophelia data is not included in the original ELDORA dataset introduced prior and the manual QC was carried out by one person who may have slight differences in technique as compared to different experts used to train the model in the original varied ELDORA training set. To gain more insight into these results and how the model used the given predictors, histograms were created for the top 6 predictors by feature importance rank (Fig. 2.3) using a probability density function (PDF) which sums to one. The data was grouped by both correct and incorrect predictions of weather and non-weather creating four different histograms for each predictor.

The behavior observed for both values of NCP and averaged NCP are similar (Fig. 2.3a,c). Correct predictions of both good and bad data cluster near high and low bounds. Low standard deviations of velocity typically indicated good data while higher values tend to be non-weather (Fig. 2.3b). Incorrect classifications for all of the top 3 predictors are concentrated in a wide range between these extremes where they are unlikely to serve as useful standalone predictors. Probability of ground gates is only a useful metric near the surface where values are non-zero. All points were the calculated probability was zero were filtered out before calculation of the PDF. All PDFs for this predictor clustered near zero indicating the challenging nature of making predictions where the probability of ground was low but non-zero. Values above 0.5 are almost exclusively true non-weather predictions (Fig. 2.3d). Good performance at high values indicates the success of the model in removing more obvious ground with the help of the predictor. Non-weather gates tend towards negative values of reflectivity and weather gates towards positive values (Fig. 2.3e). The greatest concentration of true weather predictions had positive reflectively values with a peak at 0 dBZ. Implications of PDFs from the standard deviation of reflectivity are difficult to discern (Fig. 2.3f). The ambiguity of the sixth ranked predictor which has a feature importance score close to its neighbors in the rankings and frequent overlapping of histograms suggest the importance of using several predictors together in successful QC. The PDFs of all of the six analyzed predictors do not reveal clear and decisive cutoffs providing further evidence of the shortfalls of a rules-based approach with fixed thresholds.

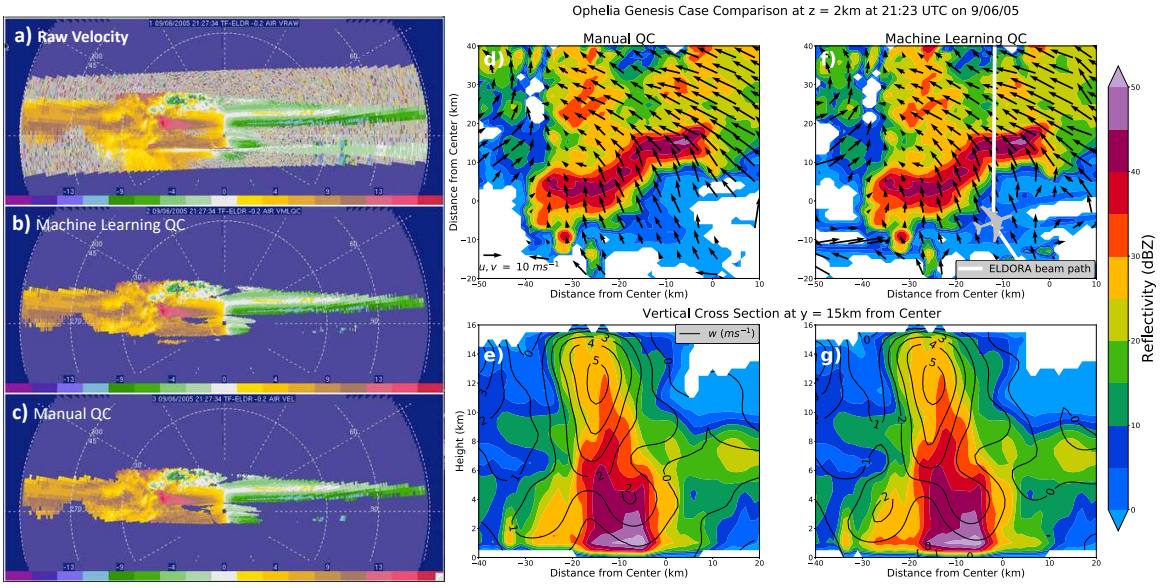

FIG. 2.4. A forward scan from ELDORA showing the a) raw, b) machine learning QC, and c) manual QC velocity fields. The path of the beam from this scan is shown as a white line. d) Top down reflectivity and the u and v wind components at 2km altitude after manual QC as vectors. e) A vertical cross section taken west to east through the most intense convection shows the vertical wind component (contours). The g) vertical cross section and f) top down reflectivity from analysis created using the RF model.

The end goal of airborne radar QC is a dual-Doppler analysis from intersecting fore and aft pointed alternating scans taken from the aircraft of the target of interest. The three dimensional variational technique SAMURAI yields a maximum likelihood estimate of the atmospheric state for given observations. SAMURAI was used to create analyses of the convective feature using scans prepared by both QC methods (Bell et al. 2012). The two methods produced a similar end product for a sample fore facing scan of velocity from the Ophelia test case provided to demonstrate how the model performs on individual scans. The main difference was a subterranean echo left by the ML method (Fig. 2.4b). The subterranean echoes may be a byproduct of the balanced class weights chosen for the model as it occurs in many other scans. Weather data is less common than non-weather in the training set which causes prioritization of the retention of weather data over the removal of non-weather. The preference for retention, combined with the low ranking of the altitude predictor in feature importance could have allowed otherwise convincing but still non-weather subterranean data to remain and decreased the percentage of non-weather data removed in the test case. The SAMURAI analyses are shown for comparison of the results obtained from each technique in Fig. 2.4. Slight discrepancies in lower reflectively values are found when comparing the top down plots in panels d and f. An inflow channel

in the bottom left corner of panel f is only present in the machine learning QC but otherwise the flow fields are largely identical. A cross section which intersects the highest reflectivity region of the convective feature along the y axis in the top-down reflectivity cross section is provided (Fig. 2.4e,f) for comparison of vertical motion. Both analyses display a similar shape and maximum value of the upward component of motion. However, there are slight differences in magnitude at the lower levels. Consistencies in the low level planar flow field (Fig. 2.4d,f) and vertical motion (Fig. 2.4e,g) indicate the method is capable of producing an analysis which would be interpreted similarly to one produced by manual QC efforts.

2.4 Conclusions

The successful use of a random forest ML model as a means to QC airborne radar data is a promising step towards reduction of effort required to perform valuable analysis. The time saved is also considerable with the automated QC running on the Ophelia pass in approximately a day compared to the minimum week of work with manual QC methods. The model performed well on its varied testing set exhibiting the ability to be a generalized method useful for several different convective feature types. Creation of a dual-Doppler analysis from previously unseen data that is comparable to manual QC efforts elevated the method to a working prototype by producing the desired end product of airborne radar QC. The complex decision making ability of ML provided an advantage over previous rules-based approaches which can fail to classify good or bad data just beyond rigid threshold values. Successful and purposefully simple hyperparameter tuning provided a blueprint for improvement of the random forest model. A more thorough tuning effort was not pursued as this experiment is a proof of concept for the ability of an automated ML technique to re-create manual efforts. A test with data collected during the 2018 hurricane season by the TDR aboard NOAA Hurricane Hunter P3 aircraft has also shown encouraging results. Details of the test are available in the following chapter. Success of the test demonstrated adaptability to newer radars thanks to its point wise classification which uses predictors universal to current airborne radars. The data mining infrastructure also allows for future additions such as dual-polarimetric radar variables as predictors when they become available. Continued effort should focus on expanding the dataset and adjusting hyperparameters and class weights to increase performance and generalization ability. The replacing of manual QC methods with automated ML would allow meteorologists to focus more time on analysis of convective phenomenon rather than on manual QC of data.

CHAPTER 3

VERTICAL DEVELOPMENT OF THE VORTICITY TOWER IN HURRICANE MICHAEL (2018)

3.1 INTRODUCTION

As large strides have been made in improving track forecasts by NOAA's National Hurricane Center (NHC), intensity forecast improvements lag behind. Improvements have been made in intensity forecasts in recent years, but were slowest to occur in the 24 to 48 hour forecast periods (DeMaria et al. 2014). The NHC defines rapid intensification (RI) as an increase in the maximum sustained winds of a tropical cyclone (TC) of at least 30 knots in a 24 hour period. Struggles in the near-term time frame can produce large errors during RI. From 1989-2018, RI was successfully predicted approximately 3% of the time in the Atlantic basin. Further improvements to intensity forecasting depend in part on better prediction of rapid intensity changes that cause larger errors explaining roughly 20% in the yearly mean absolute errors in intensity forecasts over the same time period (Trabing and Bell 2020). Hendricks et al. (2010) quantified the impact of environmental factors on TC intensity change and concluded that RI is mostly controlled by internal dynamical processes. Internal processes differentiate a gradually intensifying storm from one undergoing RI in similarly favorable environments for intensification.

TC intensification is a cooperative process between cloud-scale moist convection and cyclone-scale circulation that allows heat and moisture form the ocean to be utilized for TC growth and maintenance (Ooyama 1969). Increasing net vertical mass flux in the inner core due to the secondary circulation composed of inflow at the surface, upward motion in the eyewall, and outflow aloft is an essential component of strengthening (Ooyama 1982). More current investigation of TC intensification has placed emphasis on cloud-scales within the storm. In the beginning of the TC life cycle, intense individual convective elements termed vortical hot towers (VHTs) pre-condition the TC environment by tilting and stretching vorticity. VHTs facilitate convergence of angular momentum in the lower levels and latent heat release as a source of warming near the disturbance center (Hendricks et al. 2004). Genesis can be accomplished by the merger and axisymmetrization of VHTs which can create a system-scale circulation (Montgomery et al. 2006). Discrete convective elements remain important to the TC intensification process as it progresses towards RI. Many deep convective towers locally amplify rotation in the TC at the onset of RI, but decrease in number as RI proceeds (Van Sang et al. 2008). A composite study of aircraft reconnaissance grouped observations in intensifying and steady state hurricanes to identify differences between the groups (Rogers et al. 2013). Anomalous convective updrafts with high

local vertical velocities termed convective bursts (CBs) occurred with greater frequency and were preferentially located within the radius of maximum wind (RMW) in the intensifying storms. Convection within the RMW has been shown in theoretical work to favor RI as well (Vigh and Schubert 2009).

Simulation of RI indicated a synergistic relationship between CBs and the background secondary circulation. CBs enhance mass flux prior to RI before increased mass flux is accomplished by updrafts more representative of average vertical motion in the inner core (Rogers 2010). The transition in intensification from discrete CBs to the more axisymmetric secondary circulation is also hinted at in the composite study of aircraft observations. Intensifying storms in the study exhibited ring-like vorticity focused inside the RMW and stronger axisymmetric projections of upward motion (Rogers et al. 2013). The greatest contribution to intensification comes from the axisymmetric projection of the heating (Nolan et al. 2007) which is co-located with the eyewall updraft in a TC inner core. Updraft mass flux also peaked at higher altitudes and decreased less rapidly with height in the intensifying storm composite observations when compared to steady state. A preference towards mass flux peaks at greater elevation suggests the vertical extent of inner core eyewall convection may also be important to intensification.

Near-surface processes are also important to the spin-up of the maximum tangential winds in a TC. Intensification occurs in the frictional boundary layer when radial inflow becomes strong enough to converge angular momentum faster than it can be lost to friction (Montgomery 2016). Previous studies have examined upper level processes during RI, but there is a lack of consensus on their role in the literature. Simulation of RI in Hurricane Wilma (2005) suggested the importance of the formation and location of the upper level warm core strengthened through subsidence from deep asymmetric CBs (Chen and Zhang 2013). A double warm core structure has also been simulated with the strongest warming located in the mid-level maxima (Stern and Zhang 2010). Although both studies show upper level warming, with differing importance assigned to it, arguments have been made that the height of the warm core is not related to intensity (Stern and Nolan 2012). However, warming higher up in the atmosphere can be more efficient at lowering surface pressure (Hirschberg and Fritsch 1993).

More detailed inner core information is required to improve skill in the prediction of RI (Kaplan et al. 2010). Research flights utilizing tail Doppler radar (TDR) have been a crucial asset to furthering our understanding of inner core processes in TCs. TDR data during the RI of Hurricane Patricia (2015) to record-setting intensity documented an intense axisymmetric inner core extending deep into the troposphere (Rogers et al. 2017). Analysis of Patricia focused on evolution in a potential vorticity

framework rather than vorticity, but emphasis was placed on the axisymmetric mode of intensification (Martinez et al. 2019). Axisymmetric mechanisms have also been shown in theory to be capable of rapid strengthening of the TC warm core (Vigh and Schubert 2009). TDR data and theory were used to evaluate conventional wisdoms pertaining to the vertical structure of the tangential wind field in a TC (Stern and Nolan 2009). Despite useful findings on the slope of the RMW, questions remained about decay of the tangential wind field in the upper levels where past observations had been more sparse. A combination of a 14 dB increase in sensitivity (AOC 2016) of the TDR flying aboard the NOAA P3 Hurricane Hunter Aircraft during the 2018 Atlantic Hurricane Season, and the excellent data coverage during RI of Hurricane Michael allowed for detailed observation of the upper levels. Asymmetric contributions to RI have already been investigated in radar observations of Hurricane Michael (Cha et al. 2020). This study is focused on investigating the axisymmetric dynamical aspects of vertical growth of the vorticity tower of Hurricane Michael and inferring connections of upper level processes to RI of the near-surface wind field.

3.2 Synopsis of Hurricane Michael and observation periods

The tropical depression which developed into Hurricane Michael was first designated by the NHC on 0600 UTC 7 October about 130 nautical miles south of Cozumel, Mexico. The genesis occurred in a large area of disturbed weather in the Western Caribbean Sea. The disturbance was composed of the remnants of Tropical Storm Kirk, a surface low formed via convective bursts, and a larger cyclonic gyre. Moderate vertical wind shear present in the surrounding environment failed to prevent intensification of the system and RI began immediately. Michael attained tropical storm status 6 hours after formation and hurricane status a day later.

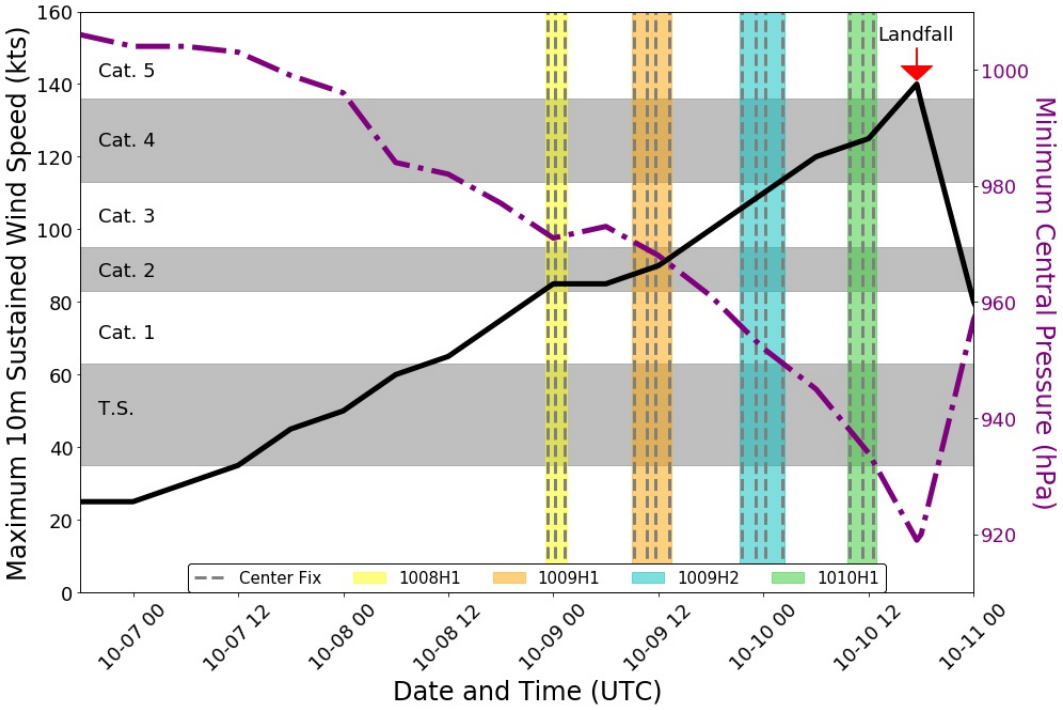

FIG. 3.1. NHC Best Track maximum sustained wind (kts) and minimum central pressure (hPa) from genesis through shortly after landfall. Observation periods by the P3 research aircraft are highlighted with embedded dashed lines indicating the time at which the aircraft reached the center during each pass through Hurricane Michael.

A brief pause in intensification took place on 8 October near the Western tip of Cuba as Michael entered the Southern Gulf of Mexico via the Yucatan Channel. During the pause, reconnaissance performed by the NOAA P3 research aircraft began. Per NHC Best Track data, the initial flight sampled Michael at category 2 intensity with maximum sustained winds of 85 knots. Michael, under the steering influence of a ridge and mid-latitude shortwave trough, took a general northward motion through the Gulf of Mexico. Intensification resumed on 9 October and continued until landfall. Two aircraft missions on 9 October captured the storm as an intensifying category 2 and a major category 3 hurricane which attained category 4 status during observation. A final NOAA mission on 10 October observed the then category 4 Hurricane Michael as it continued to intensify on approach to land. Details of the time spent in storm by the P3, center fix times of passes through the storm, and their temporal position relative to the storms changing intensity are shown in Fig. 3.1.

Landfall took place at 1730 UTC on 10 October near Tyndall Air Force Base in the Florida panhandle. Minimum central pressure was recorded at 919 hPa with maximum sustained winds estimated at 140 knots. Michael became the fourth storm to make landfall in the mainland United States (US) at

category 5 intensity. The storm caused extensive damage, most notably in the immediate coastal communities of Panama City and Mexico Beach, the latter of which was impacted by catastrophic storm surge reaching up to 14 feet above ground level. The storm's damaging trek continued inland across the Southeastern US as Micheal maintained category 3 intensity while crossing the southwest Georgia border, making it the first major hurricane to impact the state since 1890 (NWS 2019). The storm tracked through North Carolina, South Carolina, and Virginia while undergoing extratropical transition before re-emerging over the Atlantic. Hurricane Michael caused $25 billion in damage in the US and is directly responsible for 16 deaths (Beven et al. 2019). The destruction left in the wake of the storm which formed and intensified to a category 5 within four days underscores the importance of research on RI of TCs.

3.3 Data and methodology

3.3.1 Airborne radar data

The expansive temporal coverage of aircraft observations in Hurricane Michael collected by the NOAA Aircraft Operations Center provided an excellent dataset with which to examine the RI process in TCs. Four P3 missions produced fourteen passes with adequate data coverage through the core of Hurricane Michael. During each pass, the tail Doppler radar (TDR) employed a scan strategy which alternated between the fore and aft directions to produce pseudo-dual-Doppler measurements. Passes were separated by approximately an hour with the time between center fixes not exceeding 2 hours except between missions. 30 minutes of TDR data provided enough coverage to create an analysis of the inner core of Michael during a pass. Details of the duration and center fix times of each pass are listed in Table 1. The data collected spans approximately a day and a half as the storm continued to intensify and improve its structure prior to landfall.

Dual Doppler analyses

Dual Doppler analyses were created for each pass with Spline Analysis at Mesoscale Utilizing Radar and Aircraft Instrumentation (SAMURAI) software (Bell et al. 2012; Foerster and Bell 2017). The three dimensional variational data assimilation technique uses radar observations and cubic b-splines to produce a best guess at the most likely state of the atmosphere by minimizing a cost function. The retrieval technique yields the kinematic fields of the storm output in a NetCDF format. 1km horizontal and 0.5 km vertical resolution were afforded due to the close range observations collected by the TDR inside the storm. To minimize issues from attenuation and range of the X-band (3-cm wavelength)

TABLE 3.1. Times associated with each aircraft pass duration and center fix during the observational periods of the four NOAA P3 aircraft missions into Hurricane Michael.

Aircraft Mission	*Date*	*Duration (UTC)*	*CenterFix (UTC)*
1008H1	8-Oct	23:05 - 23:35	23:19
	9-Oct	00:00 - 00:30	00:15
	9-Oct	01:00 - 01:30	01:14
1009H1	9-Oct	08:57 - 09:27	09:12
	9-Oct	10:25 - 10:55	10:40
	9-Oct	11:26 - 11:56	11:41
	9-Oct	12:58 - 13:28	13:13
1009H2	9-Oct	21:14 - 21:44	21:29
	9-Oct	22:52 - 23:22	23:07
	10-Oct	00:00 - 00:30	00:15
	10-Oct	01:55 - 02:25	02:10
1010H1	10-Oct	09:35 - 10:05	09:49
	10-Oct	11:00 - 11:30	11:17
	10-Oct	12:15 - 12:45	12:30

radar, analysis was limited to the innermost 60km of the storm to capture the evolution of the inner core. Reflectivity cross sections during the first and last pass of each of the four missions (Fig. 3.2) show the changes in radar presentation and organization of the storm's inner core as it underwent RI in the Gulf. Cross sections were taken at 6 km to place emphasis on the increasing organization higher up in the storm rather than near-surface. Increases over time of symmetric coverage of high reflectivity values which denote intense convection are indicative of an intensifying storm. The increasing symmetry is important to findings of this study. However, asymmetric aspects of Hurricane Michael's evolution evident on coastal radar are also of importance and have been discussed by (Cha et al. 2020). Axisymmetric contributions to the RI process are the focus of this analysis.

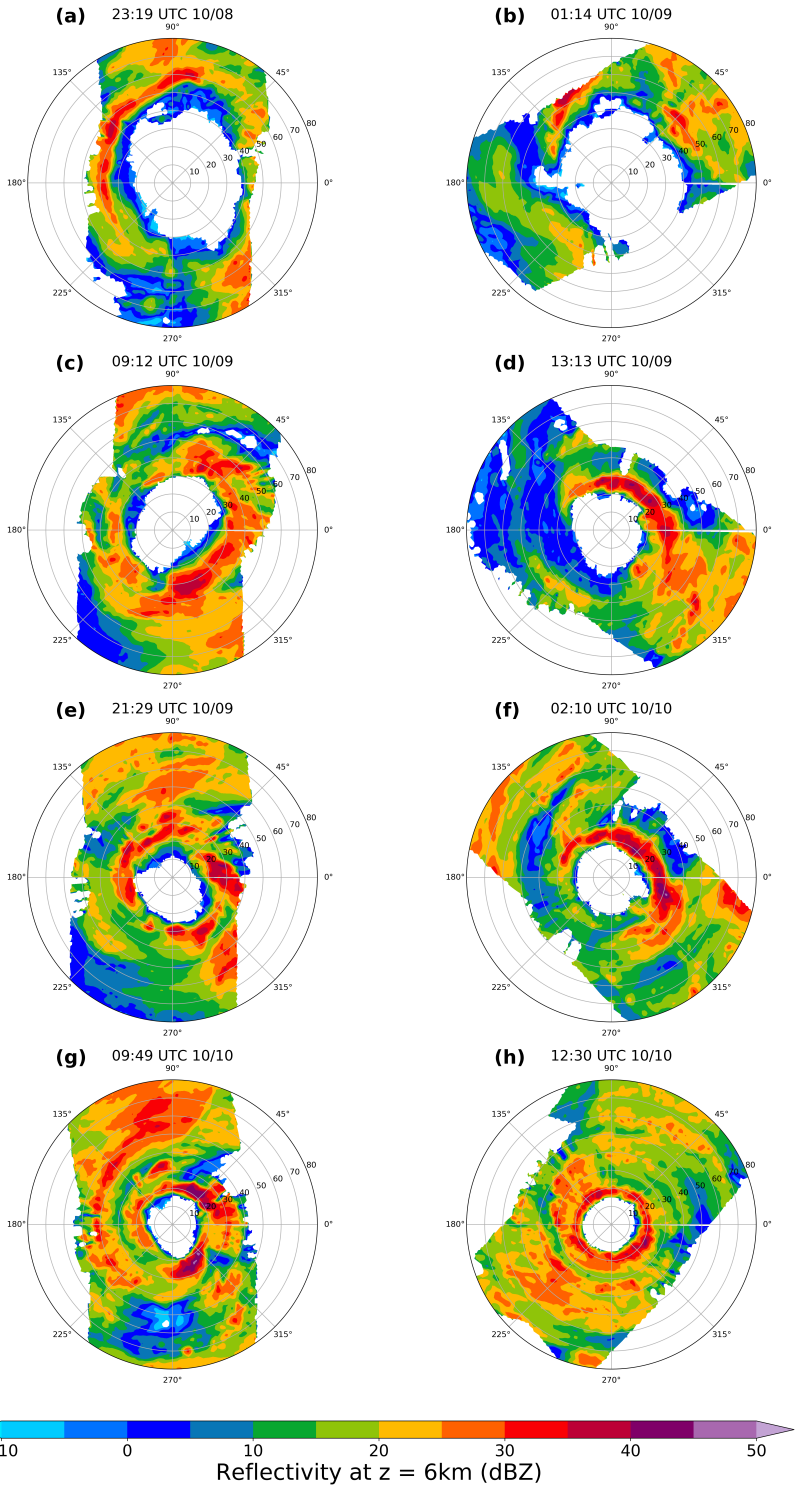

FIG. 3.2. Polar plots of radar reflectivity at 6km. The first and last aircraft pass from 1008H1(a,b), 1009H1 (c,d), 1009H2 (e,f), and 1010H1 (g,h) are shown with center fix times displayed at the top of each panel.

3.3.2 Radar quality control (QC)

Thorough QC efforts were necessary to remove non-weather echoes and prepare the raw TDR data for analysis in SAMURAI. Navigation errors introduced by movements of the aircraft within the storm and uncertainties in the inertial navigation system were corrected to obtain more accurate Doppler velocity (Cai et al. 2018). Subsequently, data from each radar scan were given an initial QC effort by the algorithm developed by Bell et al. (2013) that operates within the SOLO II radar editing software from the National Center for Atmospheric Research (Oye et al. 1995). The algorithm is a first step to successful removal of noise, ground clutter, second trip echoes, and other non-meteorological data which can prevent accurate wind synthesis from TDR data. Velocity unfolding, which is necessary in a hurricane where wind speeds exceed the Nyquist velocity of the TDR, is included in the algorithm. Even after automated QC, some manual effort was required to produce an accurate dual-Doppler wind synthesis. Two missions, originating on 08 October and 10 October, received manual QC. The time consuming nature of manual QC created a need to expedite the manual QC step of the process in order to analyze all available aircraft passes. A dataset composed of the post manual QC TDR scans from the 3 passes during the 10 October flight was compiled to produce a machine learning model capable of re-creating manual QC using the framework outlined in Chapter 2. After initial testing to set model parameters and improve accuracy, data from the first and third passes were used to train the model while witholding data from the second aircraft pass for subsequent evaluation. The model was tasked with performing QC on the second pass through Hurricane Michael on 10 October which it had not seen during training. A brief spot check for any data that should have been removed by the model was performed to investigate how close the less time consuming QC method could mirror the already completed manual effort. SAMURAI analyses were produced from the data cleaned by the model, data that received a subsequent spot check, and the original manual effort. All three analyses were compared to determine if the method could be used to QC data from the remaining two flights. The wind field obtained via machine learning QC was found to be qualitatively similar to manual QC. The wind field after an additional spot check was nearly identical to manual QC. Secondary circulation vectors and tangential wind field shown in Fig. 3.3 confirm these similarities. Successful completion of the test allowed for the QC of remaining TDR data from both missions on 9 October with the machine learning model. Approximately 30 minutes per pass of additional spot checks were performed on all passes that received model QC to maintain a similar standard of QC across the dataset. A more generalized version of this QC method was discussed in the prior chapter.

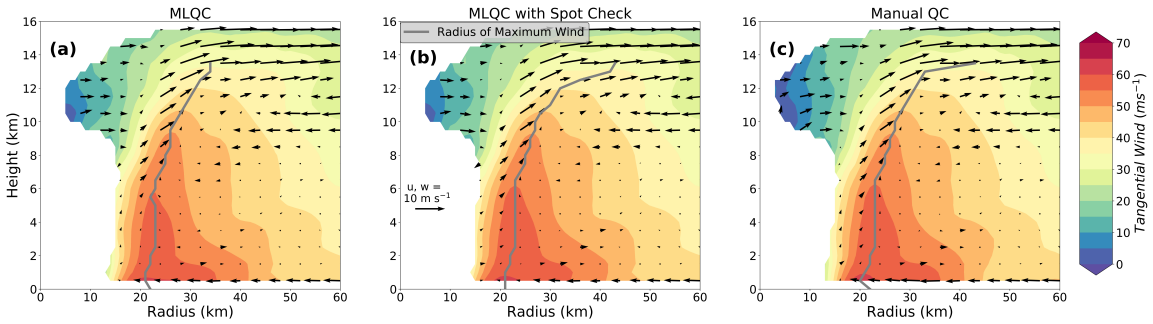

FIG. 3.3. SAMURAI analyses created from TDR data with a) machine learning QC, b) an additional spot check, and c) the original manual effort. Secondary circulation vectors show the radial and vertical components of the wind field. The tangential wind field is shown in color. RMW is contoured in gray in all panels.

3.4 INNER CORE CHANGES THROUGHOUT RI

The SAMURAI analyses captured the structural evolution of the inner core of Hurricane Michael during RI. Plots which capture the mean quantities in the azimuth dimension on the axes of radius and height are used to show changes. The radius of the azimuthal mean plots extends to 60 km with the innermost 40km having nearly complete coverage from the TDR in the azimuth dimension as evidenced by the top down radar reflectivity cross-sections (Fig. 3.2). To prevent isolated data points from biasing values, a 50% filter was used when calculating the azimuthal mean. The 50% threshold was chosen based on allowable gap size in observations that preserve wavenumber 0 axisymmetric structure (Lorsolo and Aksoy 2012). To apply the filter, each analysis file was re-gridded to a polar coordinate system consisting of radius, azimuth, and height. A mean value was only calculated for a radius height coordinate pair if data was available at 50% of the points around the azimuth. Azimuthal mean plots illustrate the evolution of changes in Hurricane Michael's average inner core structure as RI progressed. The availability of fourteen passes allowed for detailed documentation of the inward progression of angular momentum surfaces and growth of the wind field. Absolute angular momentum (AAM) is calculated from SAMURAI output using the following equation in polar coordinates where f is the Coriolis force, v_t is tangential wind, and r is radius from storm center.

$$AAM = r\,v_t + \frac{1}{2} f\,r^2 \tag{3.1}$$

Tracking of the $1.0\text{x}10^6 \text{m}^2\text{s}^{-1}$ AAM contour during each pass in of Fig. 3.4a gives an example of how an individual azimuthally averaged surface changed within the storm during each pass. The surface moved radially inward, became more vertical, and was increasingly vertical at higher altitudes with

time. The behavior of an individual AAM surface provided evidence for continual concentration of higher AAM values towards the storm center. The changing tangential wind field is documented in Fig. 3.4b by tracking the changes in the hurricane force (33 m s^{-1}) wind contour. As RI proceeded, hurricane force winds extended further radially outward from the center and increase in depth through the troposphere. The contour outline became broad and smooth in response to these changes in area of hurricane force winds in the vortex.

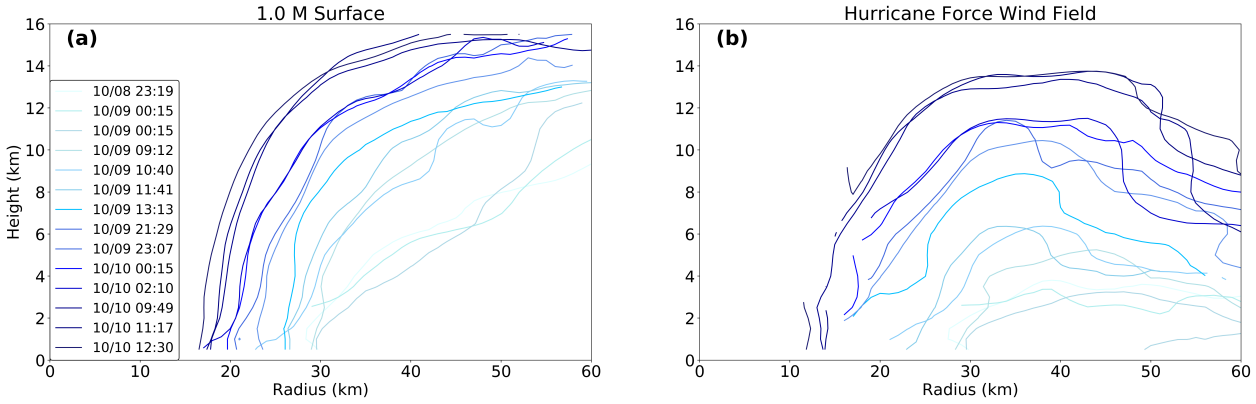

FIG. 3.4. Progression of the azimuthally averaged a) 1.0 M ($10^6 m^2 s^{-1}$) and b) hurricane force (33 m s^{-1}) wind contours during each of the fourteen passes through the storm. Increasing area of hurricane force winds and vertical nature of AAM surfaces are evident during intensification.

3.4.1 Changes in vorticity and angular momentum

Vertical vorticity and angular momentum changes during each of the four aircraft missions were calculated. Flights took approximately 2-5 hours between the first and last center fix of each depending on the amount of time spent in storm by the P3 highlighted in Fig. 3.1 . Changes in AAM (Δ M) are determined by a point subtraction method and normalized to hourly rates by taking the difference between the center fix times of the first to last pass in hours:

$$\frac{\Delta M}{\Delta t} = \frac{AAM_{Last} - AAM_{First}}{t_{Last} - t_{First}} \tag{3.2}$$

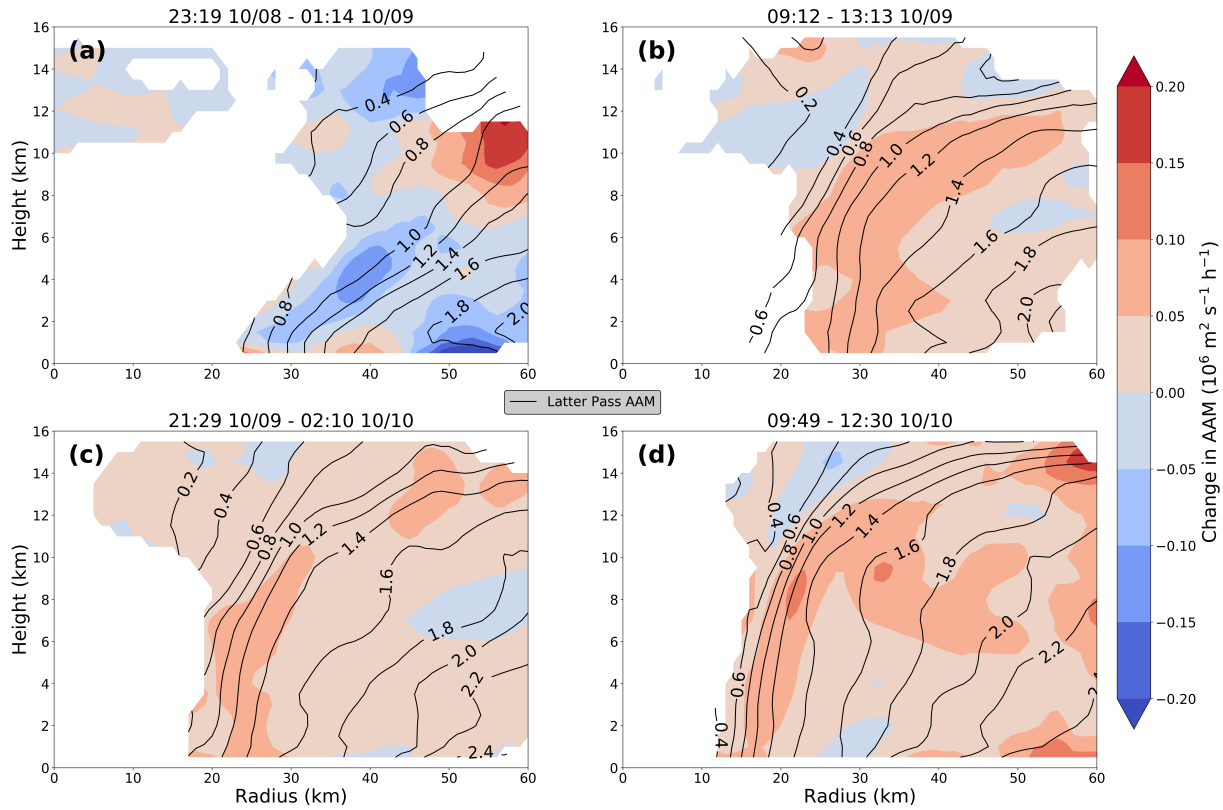

FIG. 3.5. Δ M per hour from the first to the last center fix of each aircraft mission. Contours show the AAM structure of the final fix. Warm colors indicate increasing AAM values. Differences are calculated during (a) 1008H1, (b) 1009H1, (c) 1009H2, and (d) 1010H1.

Point subtraction finds the change in AAM per hour at each radius height coordinate pair between the first and last center fixes of an aircraft mission. Contours of the AAM surfaces during the final pass in each panel show the resulting structure after changes. The calculated changes in AAM (Fig. 3.5) shown in color illuminate key changes throughout RI. AAM changes during 1008H1 in Fig. 3.5a are rather modest and disorganized. Over the following three missions, increases in Δ M concentrate mainly in the eyewall region with peak magnitudes in the mid-levels during the two missions in panels b and c. A weaker peak positive magnitude is observed in the final mission which extends uniformly through the bulk of the eyewall region. Consistent positive Δ M values were observed in the upper levels, where outflow occurs, during all missions. Δ M values during the final 3 missions are mainly positive quantities indicating larger values of M moving radially inward throughout the inner core of Hurricane Michael. Vertical vorticity (ζ) changes (Fig. 3.6) are determined by the same point subtraction method used for Δ M:

$$\frac{\Delta\zeta}{\Delta t} = \frac{\zeta_{Last} - \zeta_{First}}{t_{Last} - t_{First}} \tag{3.3}$$

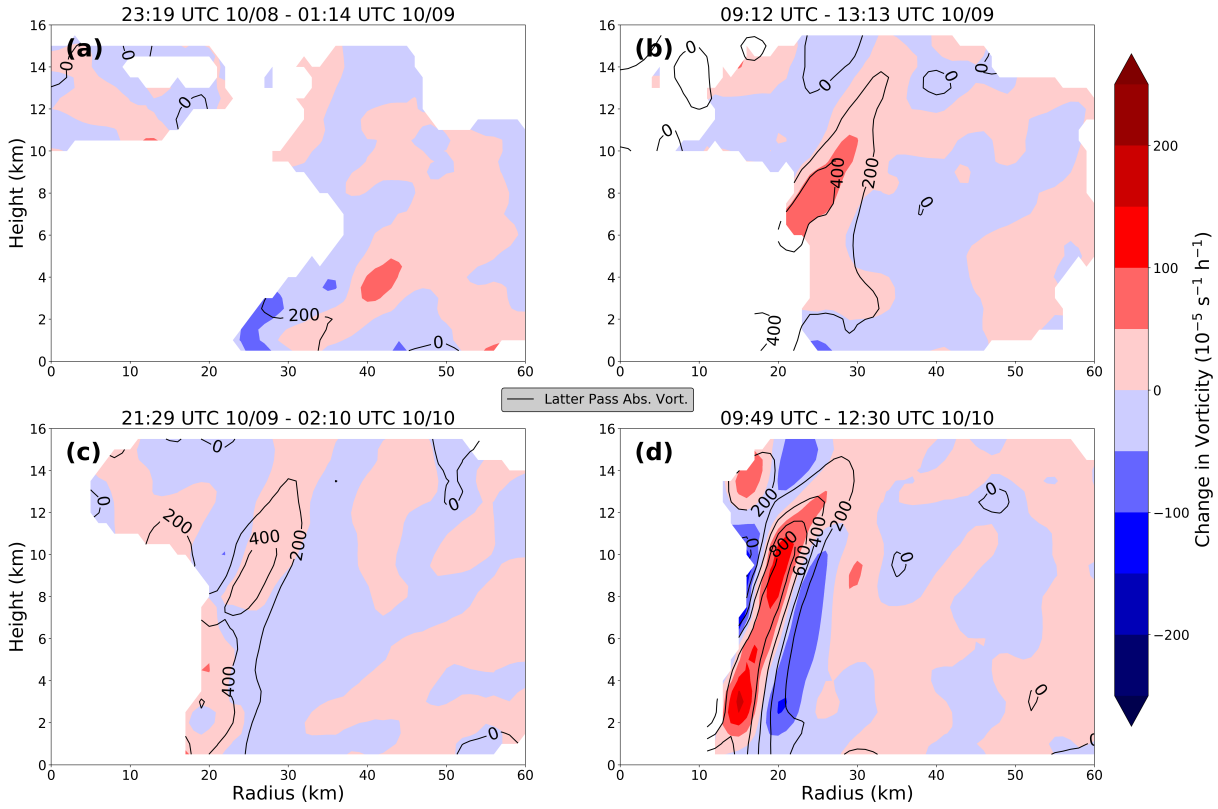

FIG. 3.6. $\Delta\zeta$ per hour shaded in color during each mission. Contours show the vorticity structure of the final fix. Warm colors indicate increasing vertical vorticity throughout the mission. Differences are calculated during (a) 1008H1, (b) 1009H1, (c) 1009H2, and (d) 1010H1.

The magnitudes of $\Delta\zeta$ per hour, shown in color, increase with time throughout intensification with the exception of a more modest increase observed during 1009H2 (Fig. 3.6c). Values of absolute vorticity observed during the last pass of each mission show the structure present after changes. The nonlinear rates with which internal organization and vertical vorticity increase are apparent when tracking changes through each mission. This observation is consistent with the rapid decrease of minimum sea level pressure, an indicator of vortex strength. The pace at which pressure fell during observation increased until landfall (Fig. 3.1) . The main region of positive $\Delta\zeta$ began as a broad outward tilted area and became more focused in the eyewall region with time. Large magnitudes of positive $\Delta\zeta$ first concentrate in the middle to upper levels in Fig. 3.6b during 1009H1. In panels c and d positive $\Delta\zeta$ begins to concentrate at all levels throughout the eyewall region with a slight lapse in the mid-levels during

1009H2 Fig. (3.6c) but a well defined signal during 1010H1 (Fig. 3.6d). During 1010H1, a strong dipole in $\Delta\,\zeta$ develops with increases in the eyewall region and decreases just outside it.

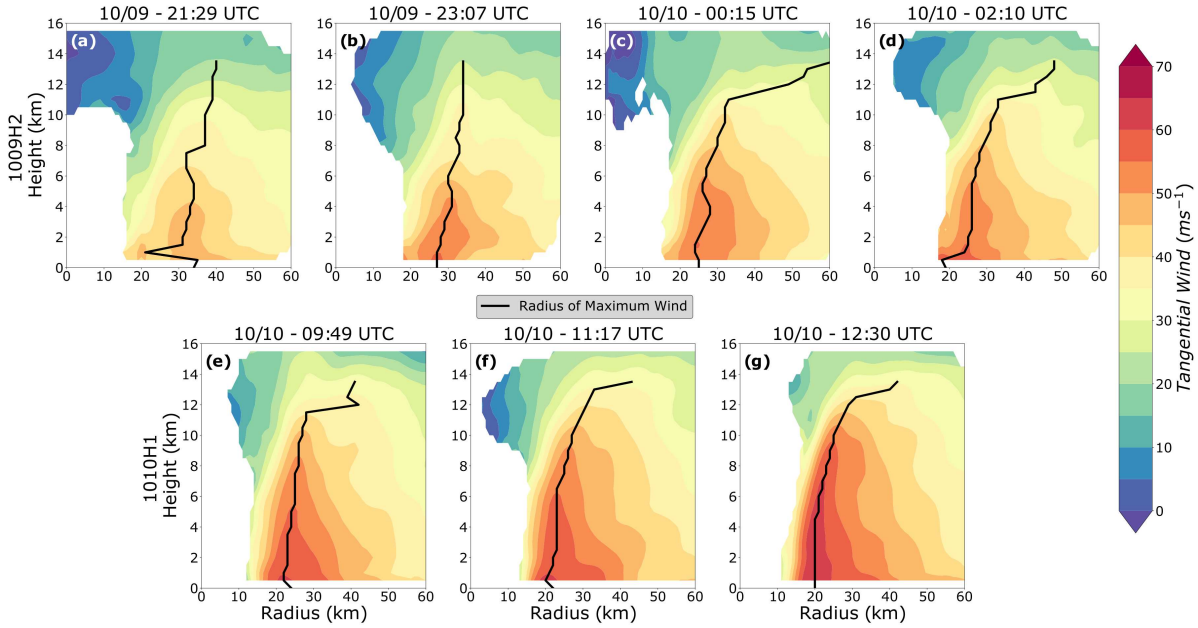

FIG. 3.7. Progression of the azimuthally averaged tangential wind field shown in color during the last two aircraft missions, 1009H2 (a,b,c,d) and 1010H1 (e,f,g), prior to landfall. The radius of maximum wind is contoured in black.

The changes observed in the inner core throughout RI paint the picture of a strengthening vortex. The expansion of the wind field was demonstrated through tracking of the hurricane force wind contour, but during the last two missions larger tangential wind values originally localized closer to the surface extend to much greater heights in the troposphere. The intensifying tangential wind field during the last 7 passes through Hurricane Michael is shown in Fig. 3.7 . Maximum azimuthally averaged values of tangential wind increased at an approximate pace of 1 m s^{-1} per hour over the course of these last two missions. The RMW also became more vertical and contracted inward as AAM surfaces did the same. The expansion of near peak tangential wind values upward is shown in Fig. 3.7g during the final pass where wind speeds within 6 m s^{-1} of the peak value (66 m s^{-1}) are found up to roughly 7 km. As the tangential wind field strengthened, the area in which it decayed rapidly with height was located at increasing heights in the vortex. The importance of tangential wind decay to observed internal processes of RI is discussed in the following section.

3.5 AXISYMMETRIC VERTICAL DEVELOPMENT OF THE VORTICITY TOWER

The latter two aircraft missions into Hurricane Michael prior to landfall documented a part of the RI event characterized by consistent vertical development of the vorticity tower in the eyewall into the upper levels. The novel and detailed look of how RI takes place in the upper levels gives a unique opportunity to diagnose mechanisms that may have been responsible. Axisymmetric dynamics played a large role in intensification during the latter two missions and a vorticity budget approach was used to identify the increasingly axisymmetric nature of Hurricane Michael's RI. Thermodynamics were also at play in the vertical expansion taking place atop the eyewall. The impacts of both dynamics and thermodynamics on storm structure are considered to evolve together as the temporal gap between observations is too great to determine if one leads the other.

3.5.1 Increasing symmetry of RI

Existing TC intensification theories focus on both axisymmetric and asymmetric modes. Studies that focus on the axisymmetric mode often build on the Sawyer-Eliassen equation (Eliassen 1952) to explain symmetric intensification in a framework termed the balanced vortex model. In the model, a forced secondary circulation comprised of lower level inflow, updrafts and latent heating near the center, and outflow aloft, becomes stronger and drives intensification (Vigh and Schubert 2009). The rotating convection paradigm seeks to explain intensification through an asymmetric process. The framework emphasizes localized rotating convective updrafts in the eyewall of a TC which enhance organization and structure of the storm's inner core (Montgomery 2016). A central difference between the two explanations lies in symmetry whereas one assumes an axisymmetric TC while the other claims the primary mechanism by which the TC intensifies to be asymmetric. The time evolution of the symmetry of intensification during Hurricane Michael's RI was analyzed with the TDR dataset. The axisymmetric relative vorticity budget equation used to analyze observations of RI in Hurricane Guillermo (1997) by Reasor et al. (2009) was employed to do so. In the following equation, prime terms denote eddy contributions that vary azimuthally while an overbar indicates an azimuthal average of the quantities below. δ is divergence, f_0 is the Coriolis parameter, and λ indicates the azimuthal dimension in cylindrical coordinates.

$$\begin{aligned}\frac{\partial}{\partial t}\bar{\zeta} = &-\bar{u}\frac{\partial \bar{\zeta}}{\partial r} - \bar{w}\frac{\partial \bar{\zeta}}{\partial w} - (f_0+\bar{\zeta})\bar{\delta} - \frac{\partial \bar{w}}{\partial r}\frac{\partial \bar{v}}{\partial z} \\ &- \overline{u'\frac{\partial \zeta'}{\partial r}} - \overline{\frac{v'}{r}\frac{\partial \zeta'}{\partial \lambda}} - \overline{w'\frac{\partial \zeta'}{\partial z}} - \overline{\zeta'\delta'} - \overline{\frac{\partial w'}{\partial r}\frac{\partial v'}{\partial z}} - \frac{1}{r}\overline{\frac{\partial w'}{\partial \lambda}\frac{\partial u'}{\partial z}}\end{aligned} \tag{3.4}$$

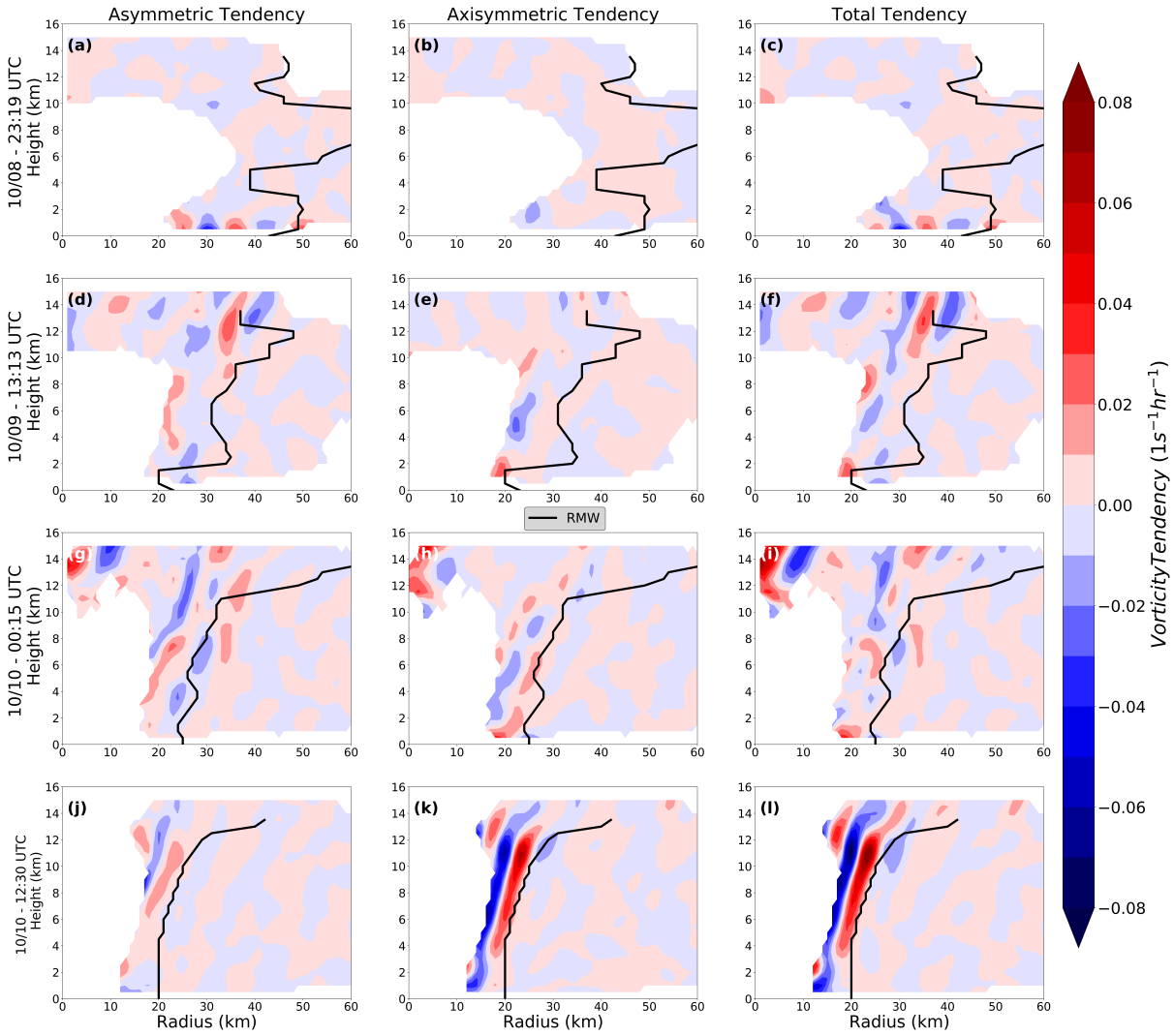

FIG. 3.8. Calculation of tendency terms in a vorticity budget exhibiting the symmetric and asymmetric contributions to Hurricane Michael's total vorticity tendency over time. The four passes are approximately 12 hours apart with center fix times shown to the left of each row. A representative pass was chosen from the (a,b,c) 1008H1, (d,e,f) 1009H1, (g,h,i) 1009H2, and (j,k,l) 1010H1 aircraft missions.

The first line of Equation 3.4 is composed of four terms which quantify the vertical vorticity tendencies associated with axisymmetric radial advection (1), vertical advection (2), stretching (3), and tilting (4). A summation of these first four terms gives a total axisymmetric vorticity tendency at the time of an aircraft pass. The second line of the equation is made up of four terms (5-8) corresponding to the same aforementioned tendencies but instead as asymmetric eddy contributions. Terms 5 and 8 are composed of two expressions. Summing these second line terms yields a total asymmetric vorticity tendency. Each of the individual axisymmetric tendency terms of the vorticity budget and how

they relate to this RI case are addressed in the discussion section. A sum of all terms in the budget produces a total vorticity tendency for both modes at the time of the analysis. These three summation values were compared in a radius and height coordinate space to show the contribution of each mode to the total tendency. A pass from each mission was chosen to represent the RI process as it proceeded from a mainly asymmetric to mainly axisymmetric mode (Fig. 3.8). The increased symmetry is most evident in the passes from the first and last missions. Fig. 3.8a and c are nearly identical as asymmetric vorticity tendency terms governed changes occuring on 08 October. Fig. 3.8k and l are nearly identical on 10 October when axisymmetric tendency terms dominated. The result of this analysis shows both schools of thought are pertinent in the RI case of Hurricane Michael. Asymmetric intensification was dominant in the beginning but an axisymmetric view of intensification became more appropriate in the later stages of RI. Mechanisms discussed in this section were observed in the latter times of RI when axisymmetric vorticity budget terms were more dominant. The following section focuses on axisymmetric dynamics to diagnose intensification.

3.5.2 *Dynamics: Contributions of Vorticity Budget Terms*

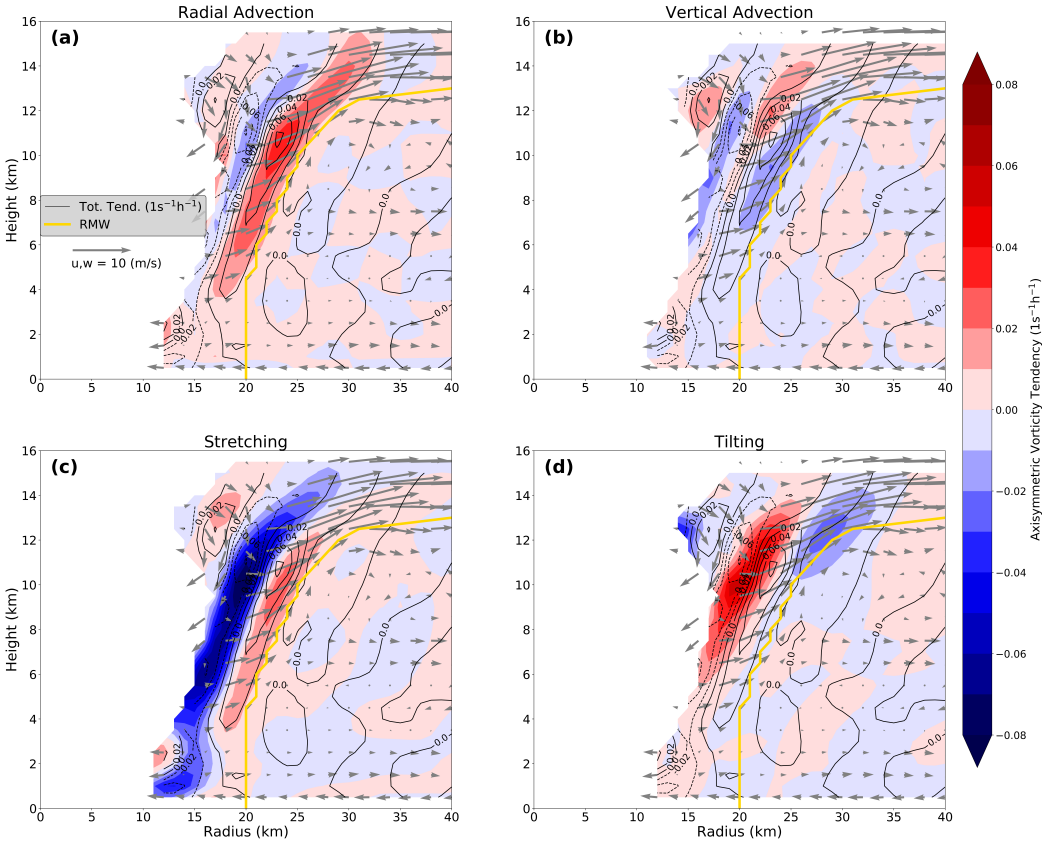

FIG. 3.9. Axisymmetric vorticity tendency terms for radial advection (a), vertical advection (b), stretching (c), and tilting (d) during the final pass through hurricane Michael prior to landfall at 12:30 UTC on 10 October 2018. The summation of all instantaneous tendency terms including asymmetric terms is contoured. The radius of maximum wind is shown in gold.

All axisymmetric terms of the vorticity budget must be considered to obtain a picture of the dynamics at play in the vertical growth of the vorticity tower. Persistent patterns were observed in the terms calculated during the latter half of Michael's observed RI. The role the terms play is shown clearly and with greatest magnitude during the last aircraft pass through Michael prior to landfall. Fig. 3.9 shows the calculated axisymmetric vorticity tendency terms from the final pass with contours of the total summation of all tendency terms in the budget. The last pass was also shown in panels j,k, and l of Fig. 3.8 which demonstrated the bulk of total vorticity tendency observed was composed of axisymmetric terms. The strong positive tilting tendency atop of the eyewall is an important piece of the puzzle, but only a small portion of it was located in a net positive total tendency region. Most of the positive tilting tendency served to offset negative effects of the stretching tendency acting to compress the tower on its

radially inward edge. Both the tilting and vertical advection tendencies built the tower vertically into the upper levels of the troposphere. The vertical expansion was accomplished through re-orientation of horizontal vorticity into the vertical and the transport of existing vertical vorticity upward by the positive vertical velocity in the eyewall. Radial advection and stretching acted together to build the tower outward along the sloped eyewall in the upper levels. The eyewall slope, which is sharper in the upper than lower levels, is expected based on the majority of cases analyzed sharing this characteristic in observations using airborne radar in Atlantic TCs (Hazelton and Hart 2013). Stretching amplified the existing vertical vorticity in the tower while radial advection moved vorticity on the inner edge of the tower towards the updraft and region of positive stretching tendency. Stretching was also increasingly effective in a non-linear fashion as the tendency depends on the present vorticity which quickly increased in the eyewall as the storm intensified. All tendency terms shown acted in concert to create a positive total tendency (contoured) slightly radially inward of the RMW.

3.5.3 *Impact of tilting*

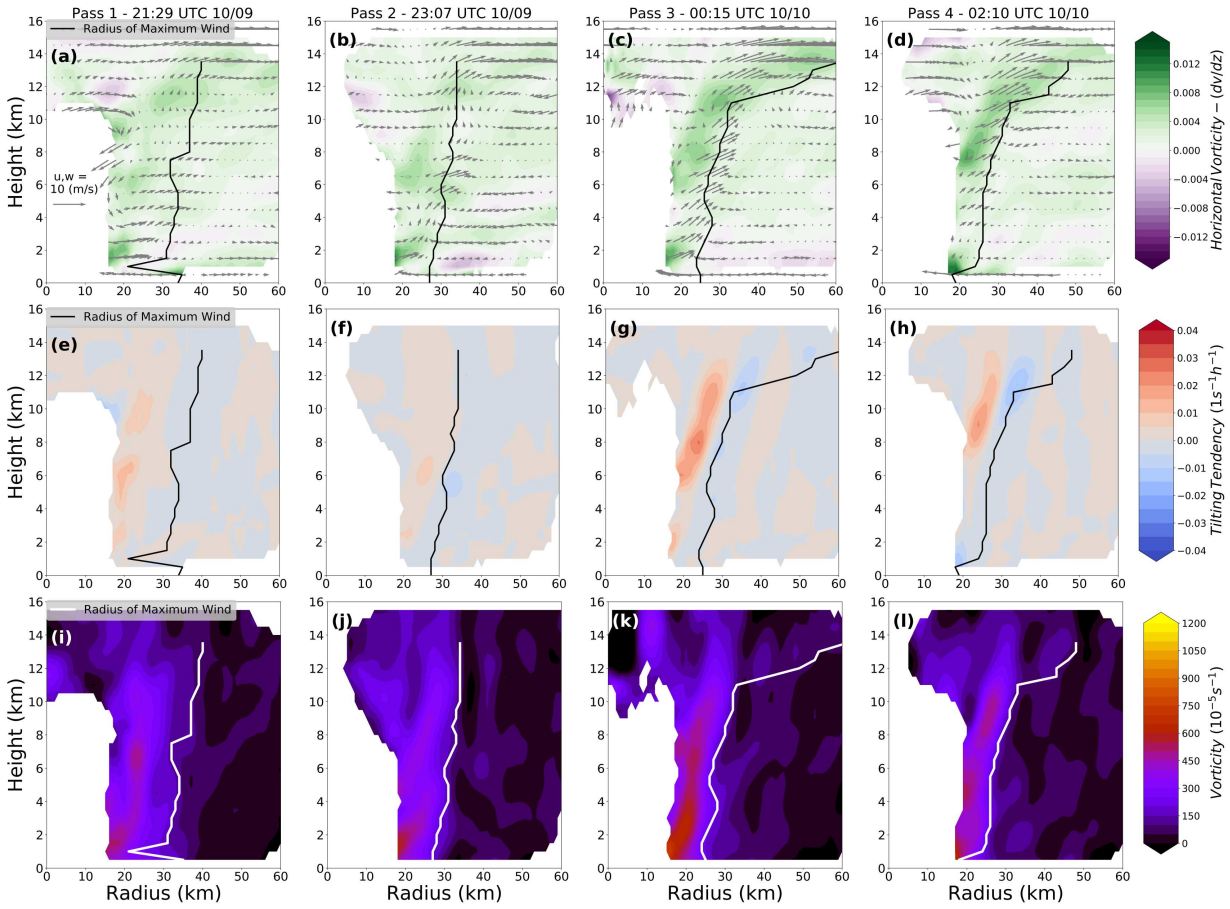

FIG. 3.10. Azimuthally averaged secondary circulation vectors with shaded horizontal vorticity values (a,b,c,d). Axisymmetric tilting of vorticity (e,f,g,h) and vorticity values (i,j,k,l) in the eyewall are shown. Analysis is from aircraft passes at 21:29 UTC (a,e,i) 23:07 UTC (b,f,j) on 09 October and 00:15 UTC (c,g,k) and 02:10 (d,h,l) on 10 October.

The contribution tilting made to storm development first became clear during the second aircraft mission into Hurricane Michael on 9 October. The azimuthally averaged evolution of the four passes from 1009H2 are shown in Fig. 3.10. In a well organized TC, wind decays rapidly with height at the top of the eyewall. Vertical decay of the wind field generated horizontal vorticity, mathematically defined as the vertical gradient of the tangential wind component, or $-\frac{\partial v}{\partial z}$. The intersection of the axisymmetric updraft, found in the secondary circulation vectors in the top 3 panels, with the horizontal vorticity, shown in color, created axisymmetric tilting tendency terms in the vorticity budget ($-\frac{\partial \bar{w}}{\partial r}\frac{\partial \bar{v}}{\partial z}$). The tendency was positive on the radially inward edge of the updraft and negative on the outer edge. The regions of positive tendency, shown in warm colors in the middle row, are areas of the storm where

the horizontal vorticity was re-oriented into positive vertical vorticity with counter-clockwise rotation. The accompanying negative dipole is due to re-orientation into negative vertical vorticity with clockwise rotation. The dipole structure between the two tendencies became more noticeable during the latter passes of 1009H2 in panels g and h. Azimuthally averaged vorticity in the eyewall of the storm showed increased magnitude where positive tilting tendencies occur. The same behavior continued with greater magnitude during the flight into Michael on 10 October prior to landfall (Fig. 3.11). Panel i shows the final observed axisymmetric vorticity tower prior to landfall exhibiting coherent and nearly uniform structure from the surface to approximately 12km.

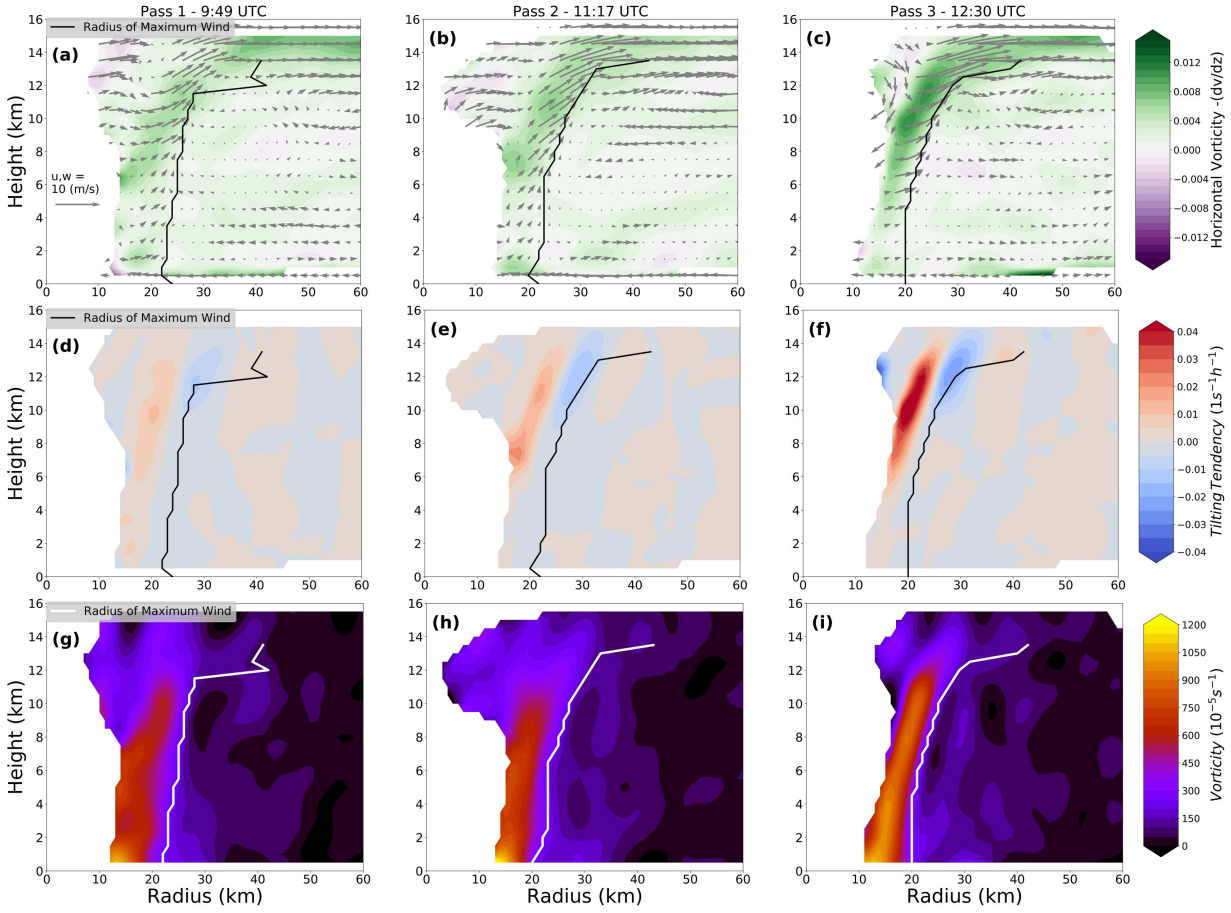

FIG. 3.11. As in Fig. 3.10 but from aircraft passes at 09:49 UTC (a,d,g), 11:17 UTC (b,e,h), and 12:30 UTC (c,f,i) on 10 October.

3.5.4 Thermodynamics: impact of thermal wind balance

Thermal wind balance in a TC can be described through a derived relationship in log-pressure coordinates from a study by Stern and Nolan (2012) where T_0 is a constant reference temperature and g is gravity.

$$(f + \frac{2v}{r})\frac{\partial v}{\partial z} = \frac{g}{T_0}\frac{\partial T_v}{\partial r} \tag{3.5}$$

Evidence for the thermal wind relationship requires a proxy for virtual temperature structure in Hurricane Michael. A method first developed by Smith (2006) permits a basic retrieval of thermodynamics from a wind field in a TC by assuming a balanced vortex and using the gradient wind and hydrostatic approximations. The method was utilized as a first step to a thermodynamic retrieval technique developed for SAMURAI by Foerster and Bell (2017) which gives a linear first-order partial differential equation that can be solved through the method of characteristics. The characteristics are the surfaces of constant pressure (Eqn. 3.6) and the variation in density potential temperature along them (Eqn. 3.7) are used:

$$\frac{dz}{dr} = \frac{1}{g}(\frac{\overline{v_t}^2}{r} + f\overline{v_t}) \tag{3.6}$$

$$\frac{\partial ln\overline{\theta_\rho}}{\partial r} = \frac{1}{g}\frac{\partial}{\partial z}(\frac{\overline{v_t}^2}{r} + f\overline{v_t}) \tag{3.7}$$

The method yields the azimuthally averaged density potential temperature ($\overline{\theta_\rho}$) which gives the azimuthally averaged density temperature (T_ρ) when multiplied by the Exner function (π). The Exner function was obtained via the gradient wind balance relationship in Exner form:

$$\frac{\overline{v_t}^2}{r} + f\overline{v_t} = c_p\overline{\theta_\rho}\frac{\partial\overline{\pi}}{\partial r} \tag{3.8}$$

Density temperature is largely similar to virtual temperature, but takes the mixing ratio of total water in all phases into account as opposed to only vapor in virtual temperature. The similarities between T_v and T_ρ make the azimuthally averaged radial gradient of $\bar{T}_\rho$, shaded in color in Fig. 3.12, a good indicator of what the radial gradient of virtual temperature may be in the inner core.

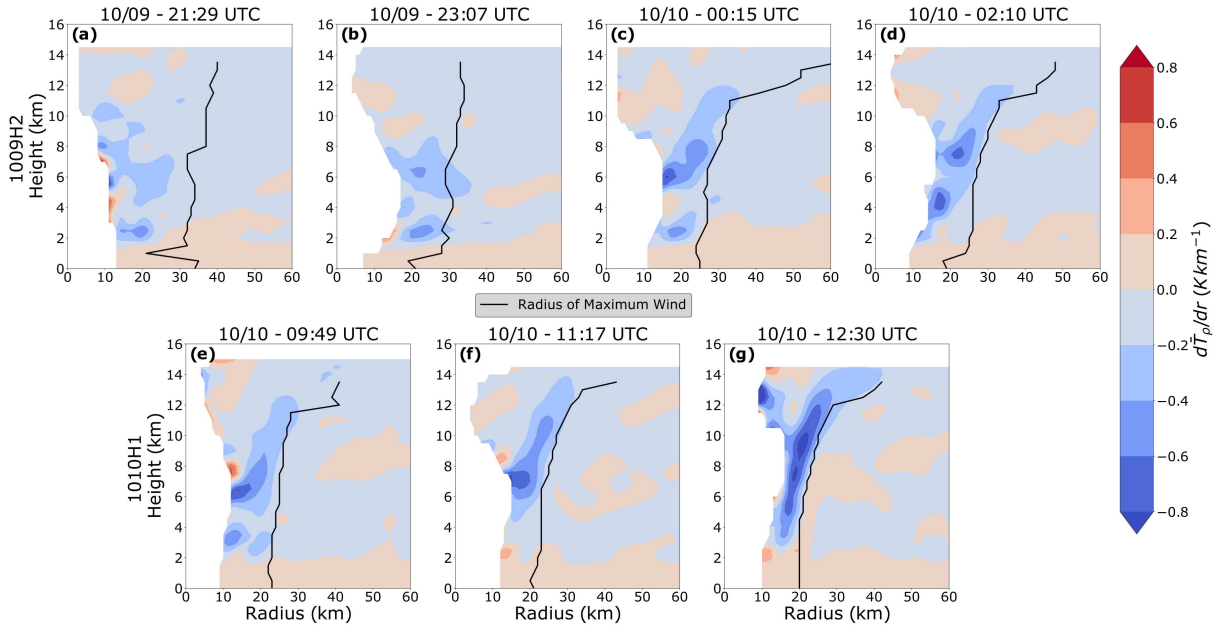

FIG. 3.12. The radial gradient of azimuthally averaged density temperature ($\bar{T}_\rho$) in the eyewall of Hurricane Michael during the last two aircraft missions prior to landfall is shown. Cooler colors indicate a negative gradient.

The increasingly negative radial gradient sets the behavior of the right hand side of Equation 3.5 as gravity and the reference temperature are constants. The balance is preserved if the opposite side of the equation is also negative and increasing in magnitude. Tangential wind in the vortex dictates the behavior of the left hand side. Changes in the tangential wind field during the last flight were given in Fig. 3.6. The increasing tangential wind ($f + \frac{2v}{r}$) was positive with increasing magnitude in the eyewall. As tangential wind values close to the near-surface maxima extended further upward into the troposphere, the vertical gradient of tangential wind ($\frac{\partial v}{\partial z}$) remained negative, but decreased in magnitude with time. The interplay between these two terms balanced the increasingly negative opposite side of the thermal wind relation both above the eyewall and within it. A point within the region of rapid vertical decay of the tangential winds maintains an increasingly negative magnitude as the sharpness of the gradient offsets the weaker winds it is multiplied by. Below the region of decay, stronger tangential winds offset the lesser magnitude of the still negative vertical tangential wind gradient. The rise of height at which the wind field decayed with each pass also raised the height at which horizontal vorticity was generated and tilted by the updraft atop the tower. Gradients considered in Equation 3.5 were not interpolated from height to the log-pressure vertical coordinate as only the overall sign and relative changes in magnitude were of importance to the qualitative analysis of mechanisms.

The cumulative picture gleaned from the analyses is of a storm that continuously tilted horizontal vorticity into the vertical at increasing heights via the eyewall updraft coupled simultaneously with the maintenance of thermal wind balance as the warm core was likely strengthening given the changes to the radial gradient of $\bar{T}_\rho$. The co-location of tilting tendencies and the increasingly negative gradient of $\bar{T}_\rho$ makes clear the interconnected nature of the dynamic and thermodynamic processes that contributed to the vertical growth of the vorticity tower in Hurricane Michael.

3.6 Discussion

The intensification of a TC via tilting of horizontal vorticity has been examined in other contexts. In cyclogenesis, transitory convective features termed VHTs tilt ambient horizontal vorticity into the vertical while also stretching the vertical vorticity from the mesoscale convective vortex they are embedded in (Montgomery et al. 2006). The short lived nature of the hot towers differs from the Michael case as the eyewall and accompanying updraft causing the tilting were axisymmetric features with a constant presence in the later stages of RI. The constancy allowed tilting to be a persistent process versus an episodic one. Tilting was identified as a contributing factor in the intensification of the secondary eyewall of Hurricane Rita (2005). The secondary eyewall case was also observed by airborne Doppler radar. A positive vorticity tilting tendency occurred radially inward of the secondary eyewall (Didlake and Houze Jr. 2011). Structural differences differentiate the Rita case from the one analyzed in Michael. The forming secondary eyewall contained embedded convective cells with higher reflectivity, which were less uniform by visual inspection than the axisymmetric convective ring observed in the mature inner eyewall of Hurricane Michael. The updraft in the secondary eyewall of Rita was centered in the reflectivity tower. The updraft in Michael's eyewall was displaced slightly radially outward of the center of the reflectivity tower co-locating the positive tilting tendency with the top of the existing vorticity tower.

Tilting was important but did not compose the whole picture of the observed inner core dynamics. The dipole nature of tilting prevents the term from increasing the net circulation on its own. Persistent patterns observed in the axisymmetric vorticity terms exhibited their greatest magnitude during the last aircraft pass through Michael prior to landfall as the storm approached category 5 intensity (Fig. 3.9). The largest magnitudes occurring at the time Michael is at peak TDR observed intensity are consistent with findings from Nolan et al. (2007) which indicated efficiency of heating in a storm increases as a vortex gets stronger. Vertical advances of the tower were accomplished by tilting and

vertical advection which re-orientated horizontal vorticity and transported ambient vertical vorticity upward with positive vertical velocities respectively. Radial advection and stretching built the tower outward along the sloped eyewall. Advection terms close the gap between tilting and stretching during the observed RI of Hurricane Michael. The negative tilting portion of the dipole is located near strong upper level outflow shown by secondary circulation vectors (Fig 3.9d) which can transport the negative vorticity out of the inner core. Advection terms transport the re-oriented positive vertical vorticity from tilting to the outer portion of the updraft region allowing for amplification through stretching which intensified the tower in the upper levels.

The total positive vorticity tendency resulting from all axisymmetric terms was located along the inner edge of the RMW where convective heating, evidenced by the updraft, took place. Convective heating in the eyewall causes thermally indirect subsidence warming inside the eye (Willoughby 1998). Towards the end of the observation period of Michael, accompanying downdrafts on the inner edge of the upper eyewall, shown by secondary circulation vectors (Fig. 3.9 and Fig. 3.10), were observed indicators of subsidence. Resulting forced dry descent as a consequence of heating in the eyewall aids in making the eye cloud free (Houze Jr. 2010), which was observed via satellite imagery showing a clearing eye during the final two missions. The descent leads to continued strengthening of the warm core. Structure, location, and intensity of the warm core could not be speculated on without thermodynamic observations available above aircraft reconnaissance flight level. However, it is reasonable to assume the warm core temperature perturbation grew in the middle to upper levels where the radial gradient of $\bar{T}_\rho$ was greatest and tilting was taking place. Warming in the upper levels impacted near-surface intensification of the vortex. In the stratospheric level of insignificant dynamics (LID) assumption, which is valid on TC scales, local temperature changes at any level above the surface and the LID contribute to the pressure tendency at the surface (Hirschberg and Fritsch 1993). Furthermore, warming in the upper levels where density is lower and there is greater spacing between isobars has a greater impact on the surface pressure than warming at lower levels would. Lower surface pressure correlates with intensification of the wind field in the lower levels due to a greater pressure gradient force.

Although the axisymmetric vorticity tower became more thinly concentrated in physical space, the angular momentum surfaces moved radially inward faster than the convective heating which is co-located with the updraft. A comparison of the tracked AAM surface in Fig. 3.4a to the secondary circulation vectors (Fig. 3.10 and Fig. 3.11) support the inward movement of angular momentum surfaces outpacing the heating. As a result, the dynamic size of heating increased along with the efficiency

of heating when considered in the potential radius framework pioneered by Schubert and Hack (1983). As the eyewall remained fixed to the inside edge of the RMW, it still moved inward towards the storm center as the RMW contracted (Fig. 3.7), a behavior also linked to subsidence in the eye (Willoughby 1998). Tendency terms in the vorticity budget indicated intensification was mainly axisymmetric in the later stages of RI, but eddy contributions were non-negligible and also played a role (Cha et al. 2020).

3.7 Conclusion

Four missions flown by the NOAA Hurricane Hunters provided an opportunity to investigate Hurricane Michael's historic RI event in the Gulf of Mexico which led to the fourth recorded landfall of category 5 hurricane in the United States. Aided by the three dimensional variational technique SAMURAI, 14 passes through the storm allowed for snapshots of the dynamics ongoing in the inner core of the storm. A detailed investigation of poorly understood inner core processes, which are a considerable hindrance to intensity forecasts for TCs, that lead to RI was undertaken. Point subtractions between analyses at the start and end of each aircraft mission quantified changes in vertical vorticity and angular momentum. Changes in both exhibited increasingly positive magnitudes which concentrated in the eyewall region as the RI event progressed. Angular momentum changes were largely positive while the vorticity changes progressed towards a dipole with positive magnitude changes in the vorticity tower and negatives just radially outside. The decrease in vorticity outside the eyewall can be partially attributed by the negative tilting tendency which accompanied the positive one, but further investigation is needed for a more complete explanation. Inward movement of angular momentum surfaces and growth of the hurricane force wind field were documented and behaved as expected in an intensifying vortex. A vorticity budget approach was used to chronicle the intensification of the storm as it proceeded towards a predominantly axisymmetric versus asymmetric mode.

Thorough temporal coverage of Hurricane Michael during RI allowed for observation of the vorticity tower as it built vertically into the upper levels of the troposphere. Tilting of the ambient horizontal vorticity, created by the decay of the tangential wind field with height, by the eyewall updraft was found to create a negative tendency radially outward of the updraft, and a positive tendency inward atop the existing vorticity tower. Tilting has been identified as an intensification mechanism in other stages of the TC life cycle, but observation of it in the upper levels of a rapidly intensifying Atlantic hurricane provide a valuable new look at the tilting process. A qualitative analysis of the axisymmetric vorticity

budget terms during the final aircraft pass paint a more complete picture of the dynamics of the intensification of the eyewall during RI. While tilting re-oriented horizontal vorticity into the vertical orientation, vertical advection aided in transporting existing vorticity from the tower upward. Stretching in the updraft region amplified the vorticity right along the inner edge of the RMW while radial advection moved vorticity from the inner edge of the tower towards the updraft region. Tilting alone cannot increase the overall circulation within the inner core, but advection of the newly oriented positive vertical vorticity to the radially outer region of the updraft allowed for it to be amplified by stretching.

The assumed maintenance of thermal wind balance during RI provided evidence of an increasing warm core temperature perturbation in the upper levels where heating can have an increased impact on surface pressure. The co-location of the radial gradient of density temperature and tilting tendency show the interconnected nature of the dynamic and thermodynamic mechanisms observed. Warming in the upper levels has a more substantial impact than warming closer to the surface on lowering the minimum sea level pressure. Connections between upper level warming and lower surface pressure allowed mechanisms of RI taking place in the upper levels to play a role in the intensification of the near-surface wind field. Hurricane Michael's well-defined axisymmetric structure shown in these analyses suggest the mechanisms explored in this study took place in a continuous and efficient manner. Observed behaviors and structure during intensification were used to corroborate previous studies related to the subject. Further investigation of the intensification mechanisms presented here through both future observations and modeling studies is recommended. Improved understanding of inner core processes which allow storms to undergo RI should aid in improving short term intensity forecasts in the future.

CHAPTER 4

CONCLUSIONS AND FUTURE WORK

As forecasting of TC track has increased markedly, the poorly understood nature of RI has hampered advances in intensity forecasting, especially in near term forecasting periods (DeMaria et al. 2014). Previous studies determined internal processes are the critical factor allowing RI to take place in a favorable environment and more detailed inner core information is required to further understanding (Hendricks et al. 2010; Kaplan et al. 2010). Data collected by the TDR aboard the NOAA P3 Hurricane Hunter aircraft coupled with the three dimensional variational technique SAMURAI (Bell et al. 2012) make detailed observation of inner core processes in storms that undergo RI possible through dual-Doppler wind synthesis. 14 passes through Hurricane Michael with adequate TDR coverage to resolve the inner core created an opportunity to document changes in the inner core and internal processes which contributed to the historic RI event that allowed a landfall at category 5 intensity in the US. A great deal of radar data QC was required to compile an accurate and thorough picture of the evolving inner core.

In order to preserve time for analysis of internal mechanisms, machine learning was explored as an avenue to automate the time-consuming and necessary manual QC of the data. Past efforts to automate QC of airborne radar data struggle from the limitations brought on by thresholding in a rules-based approach (Bell et al. 2013; Gamache et al. 2008). A random forest model was trained to clean TDR data. A training set collected by ELDORA contained scans from a tornadic supercell, bow echo, and both mature and developing TCs. Predictors collected from the training set included radar moments, mathematical quantities relating those moments to neighboring radar gates, and other specialty calculated predictors. These predictors were used to identify non-weather radar gates in the dataset that trained radar experts had removed during manual QC. The classification model accomplished this differentiation with over 99% accuracy on the previously unseen varied testing set withheld at random from the training data. The F_1 score metric, which is more suited to evaluation of binary classification with imbalanced classes, confirmed the accuracy by reporting a similar mark. Success with several different weather phenomenon at once showed promise for the method to be generalized to QC all airborne radar data collected in convective environments.

The trained model was also able to successfully QC a test case from the depression which spawned Hurricane Ophelia (2005). SAMURAI analyses produced from both automated machine learning QC

data and the original manual QC produced results with only slight differences that do not change the overall dynamics observed. Histograms of data from the Ophelia case for each of the top predictors grouped by both correct and incorrect classification of weather and non-weather gave more insight into model performance. Higher ranking predictors like NCP behaved as predicted with extreme values consistently having correct classifications and the model misses were concentrated between the extremes. Less effective predictors like reflectivity and the average of it were not as useful on an individual basis. The failure of predictors to be useful alone confirmed the need for multiple predictors to be used together in radar QC in a successful classification scheme. The radar QC framework outlined in Chapter 2 was used to create a model to perform the additional manual QC needed for Hurricane Michael after pre-processing by an initial rules-based technique. A similar test to the Ophelia case was run using Hurricane Michael data from 10 October. Successful creation of a nearly identical analysis to manual QC efforts with a brief spot check after using the machine learning model cleared the way for 8 remaining passes to receive automated QC.

Fourteen snapshots of Michael's inner core were made available for analysis by efforts of the NOAA P3 aircraft crew and QC automation which sped up the process. Retrieval of the inner core kinematics with SAMURAI and thermodynamic information from a technique originated by Smith (2006) created an opportunity for a thorough diagnosis of RI enabling mechanisms. Monitoring of evolution of the inner core revealed angular momentum values which increased in the inner core and became more vertically aligned. The hurricane force wind field expanded both radially outward and grew in depth through the troposphere. Changes in vorticity and angular momentum were calculated during each of the four aircraft missions. Changes in angular momentum were largely positive in all missions after the first. Changes in vertical vorticity became increasingly positive over time, but a dipole structure developed with losses occurring just radially outward of the large positive values in the eyewall region. A vorticity budget with both axisymmetric and eddy terms was used to evaluate the symmetry of intensification. Earlier stages of the observed RI event were mainly characterized by asymmetric eddy contributions while axisymmetric terms dominated the calculated total vorticity tendency in the later stages of RI.

Expansive data coverage of Hurricane Michael from the TDR aboard the P3 during the 2018 Atlantic Hurricane Season made detailed observations of the vorticity tower as it built vertically in the storm possible. Horizontal vorticity was generated above the eyewall by the decay of the tangential wind field with height. Tilting of the horizontal vorticity by the axisymmetric updraft present in later stages of RI

created a positive vertical vorticity tendency above the existing axisymmetric vorticity tower. Tilting as a mechanism for intensification is known to be present in other stages of the TC life cycle (Montgomery et al. 2006; Didlake and Houze Jr. 2011). However, the axisymmetric nature with which it occurred in the mid- to upper-levels of Hurricane Michael is a new finding. Analysis of persistent patterns in the axisymmetric vorticity budget terms during the end stages of RI before landfall showed a more complete picture of how the vorticity tower grew. The tilting tendency term does produce a positive tendency atop the tower, however a large portion of the positive region worked to offset negative tendencies from negative stretching acting to compress the tower on the radially inward edge of the eyewall. Tilting and vertical advection acted to expand the tower upward via the re-orientation of horizontal vorticity and transport of existing positive vertical vorticity upward in the eyewall. Radial advection and stretching built the tower outward along the RMW in the sloped eyewall by amplifying existing vertical vorticity in the updraft through stretching and moving positive vertical vorticity on the inner edge of the eyewall towards the region of positive stretching.

Thermal wind balance maintainance in the mid- to upper-levels present in the analyses provided evidence for the intensification of a warm core in the eye. An increasing negative radial gradient of density temperature suggest an increasing warm core temperature perturbation in the upper levels. Behaviors linked with subsidence warming, such as downdrafts on the inner edge of the eyewall and a clearing eye, further suggest the increasing temperatures in the eye. Co-location of the tilting tendency and maximized areas of the negative radial density temperature gradient showed the dynamics and thermodynamics of RI in the upper levels of Hurricane Michael were intertwined. Advection aided in clarifying the link betwee re-oriented horizontal vorticity at the top of eyewall and amplification via stretching. When considered with the LID approximation, warming in the upper levels aided in lowering the minimum sea level pressure of the storm at the surface center. The decrease in pressure is linked with the observed intensification of the near-surface wind field which allowed the storm to attain category 5 intensity on the Saffir-Simpson Hurricane Wind Scale. The axisymmetric nature of the mechanisms observed in the later stages of RI allowed Hurricane Michael to intensify in a manner that was both continuous and efficient.

Continued improvement of the random forest QC prototype presented here should focus on expansion of the training dataset to include more radars and weather phenomenon. Greater attention should be paid to the hyperparameter tuning process with a larger dataset to increase generalization ability of the model. The infrastructure of the framework which focuses on data mining of predictors

and making decisions on a point by point basis allow for easy implementation of new predictors when new radar platforms present them. QC of data collected in non-convective environments should be attempted to extend this method beyond the convective environments it has proved successful in. Effort should also be focused on speeding up the machine learning QC method. Most of the roughly day long run time is taken up by the data mining process which could be both edited with a focus on computational speed and parallelized. If the time the method takes could be adequately decreased, the TDR observations could be assimilated into numerical simulations which has been shown to improve TC forecasts (Zhang et al. 2012).

The observed mechanisms of RI in the upper levels as well as the link between upper-level and near-surface intensification should be investigated further in both observations and models. A less idealized and constrained thermodynamic retrieval added onto SAMURAI will be employed in an attempt to clarify the thermodynamics analyzed with more detailed information (Foerster and Bell 2017). Collection of thermodynamic information through instrumentation such as high altitude dropsondes in the upper levels of TCs would help to solidify findings in this thesis. The automation of thorough airborne radar QC should continue to de-mystify the mechanisms present during RI as it makes more detailed inner core information available to researchers in the future with less effort.

REFERENCES

AOC, 2016: Tropical cyclone operations: Challenges in 2015; new products and services planned for 2016 and 2017. NOAA Office of Marine and Aviation Operations Aircraft Operations Center, cited: 2020-09-29, [Available online at `https://www.ofcm.gov/meetings/TCORF/ihc16/2016presentations.html`].

Bargen, D. W. and R. C. Brown, 1980: Interactive radar velocity unfolding. *Preprints of 19th Conference on Radar Meteorology, Miami Beach, FL, Amer. Meteor. Soc., 1980*, 278–285.

Bell, M. M., W.-C. Lee, C. A. Wolff, and H. Cai, 2013: A solo-based automated quality control algorithm for airborne tail doppler radar data. *J. Appl. Meteor. Climatol.*, **52 (11)**, 2509–2528.

Bell, M. M. and M. T. Montgomery, 2010: Sheared deep vortical convection in pre-depression hagupit during tcs08. *Geophys. Res. Lett.*, **37 (6)**.

Bell, M. M., M. T. Montgomery, and K. A. Emanuel, 2012: Air-sea enthalpy and momentum exchange at major hurricane wind speeds observed during cblast. *J. Atmos. Sci.*, **69 (11)**, 3197–3222.

Beven, J. L., R. Berg, and A. Hagen, 2019: Hurricane michael (2018). *National Hurricane Center Tropical Cyclone Rep.*, **86**, pp. 86.

Boukabara, S.-A., V. Krasnopolsky, J. Q. Steward, E. S. Maddy, N. Shahroudi, and R. N. Hoffman, 2019: Leveraging modern artificial intelligence for remote sensing and nwp: Benefits and challenges. *Bull. Amer. Meteor. Soc.*, **100 (12)**, ES473–ES491.

Cai, H., W.-C. Lee, M. M. Bell, C. A. Wolff, X. Tang, and F. Roux, 2018: A generalized navigation correction method for airborne doppler radar data. *J. Atmos. Oceanic Technol.*, **35 (10)**, 1999–2017.

Cha, T. Y., M. M. Bell, W. C. Lee, and A. J. DesRosiers, 2020: Polygonal eyewall asymmetries during the rapid intensification of hurricane michael (2018). *Geophys. Res. Lett.*, **N/A**, N/A, doi: 10.1029/2020GL087919.

Chen, H. and D.-L. Zhang, 2013: On the rapid intensification of hurricane wilma (2005). part ii: Convective bursts and the upper-level warm core. *J. Atmos. Sci.*, **70**, 146–162, doi: 10.1175/JAS-D-12-062.1.

Claesen, M. and B. De Moor, 2015: Hyperparameter search in machine learning. *arXiv*, **https://arxiv.org/abs/1502.02127**.

DeMaria, M., C. R. Sampson, J. A. Knaff, and K. D. Musgrave, 2014: Is tropical cyclone intensity guidance improving? *Bull. Amer. Meteor. Soc.*, **95**, 387–398, doi: 10.1175/BAMS-D-12-00240.1.

Didlake, A. C. and R. A. Houze Jr., 2011: Kinematics of the secondary eyewall observed in hurricane rita (2005). *J. Atmos. Sci.*, **68**, 1620–1636, doi: 10.1175/2011JAS3715.1.

Eliassen, A., 1952: Slow thermally or frictionally controlled meridional circulation in a circular vortex. *Astrophysica Norvegica*, **5**, 19–60.

Foerster, A. M. and M. M. Bell, 2017: Thermodynamic retrieval in rapidly rotating vortices from multiple-doppler radar data. *J. Atmos. Oceanic Technol.*, **34 (11)**, 2353–2374, doi: 10.1175/JTECH-D-17-0073.1.

Gamache, J. F., P. P. Dodge, and N. F. Griffin, 2008: Automatic quality control and analysis of airborne doppler data: real-time applications, and automatically post-processed analyses for research, 28th Conf. on Hurricanes and Tropical Meteorology, Orlando, FL, Amer. Meter. Soc.

Hazelton, A. T. and R. E. Hart, 2013: Hurricane eyewall slope as determined from airborne radar reflectivity data: Composites and case studies. *Wea. Forecasting*, **28**, 368–386, doi: 10.1175/WAF-D-12-00037.1.

Hence, D. A. and R. A. Houze, 2008: Kinematic structure of convective-scale elements in the rainbands of hurricanes katrina and rita (2005). *J. Geophys. Res.*, **113 (D15)**.

Hendricks, E. A., M. T. Montgomery, and C. A. Davis, 2004: The role of "vortical" hot towers in the formation of tropical cyclone diana (1984). *J. Atmos. Sci.*, **61**, 1209–1232, doi: 10.1175/1520-0469(2004)061<1209:TROVHT>2.0.CO;2.

Hendricks, E. A., M. S. Peng, B. Fu, and T. Li, 2010: Quantifying environmental control on tropical cyclone intensity change. *Mon. Wea. Rev.*, **138**, 3243–3271, doi: 10.1175/2010MWR3185.1.

Hildebrand, P. H., et al., 1996: The eldora/astraia airborne doppler weather radar: High-resolution observations from toga coare. *Bull. Amer. Meteor. Soc.*, **77 (2)**, 213–232.

Hirschberg, P. A. and J. M. Fritsch, 1993: On understanding height tendency. *Mon. Wea. Rev.*, **121**, 2646–2661, doi: 10.1175/1520-0493(1993)121<2646:OUHT>2.0.CO;2.

Houze, R. A., W.-C. Lee, and M. M. Bell, 2009: Convective contribution to the genesis of hurricane ophelia (2005). *Mon. Wea. Rev.*, **137 (9)**, 2778–2800.

Houze Jr., R. A., 2010: Clouds in tropical cyclones. *Mon. Wea. Rev.*, **138**, 293–344, doi: 10.1175/2009MWR2989a.1.

Houze Jr., R. A., S. S. Chen, B. F. Smull, W.-C. Lee, and M. M. Bell, 2007: Hurricane intensity and eyewall replacement. *Science*, **315**, 1235–1239, doi: 10.1126/science.1135650.

Houze Jr., R. A., S. A. Rutledge, M. I. Biggerstaff, and B. F. Smull, 1989: Interpretation of doppler weather radar displays of midlatitude mesoscale convective systems. *Bull. Amer. Meteor. Soc.*, **70**, 608–619, doi: 10.1175/1520-0477(1989)070<0608:IODWRD>2.0.CO;2.

Jorgensen, D. P., T. Matejka, and J. D. DuGranrut, 1996: Multi-beam techniques for deriving wind fields from airborne doppler radars. *Meteor. Atmos. Phys.*, **59**, 83–104, doi: 10.1007/BF01032002.

Kaplan, J., M. DeMaria, and J. A. Knaff, 2010: A revised tropical cyclone rapid intensification index for the atlantic and eastern north pacific basins. *Wea. Forecasting*, **25**, 220–241, doi: 10.1175/2009WAF2222280.1.

Klotzbach, P. J., M. M. Bell, S. G. Bowen, E. J. Gibney, K. R. Knapp, and C. J. Schreck III, 2020: Surface pressure a more skillful predictor of normalized hurricane damage than maximum sustained wind. *Bull. Amer. Meteor. Soc.*, **101 (6)**, E830–E846, doi: 10.1175/BAMS-D-19-0062.1.

Lakshmanan, V., C. Karstens, J. Krause, and L. Tang, 2014: Quality control of weather radar data using polarimetric variables. *J. Atmos. Oceanic Technol.*, **31 (6)**, 1234–1249.

Lee, W.-C., F. D. Marks, and C. Walther, 2003: Airborne doppler radar data analysis workshop. *Bull. Amer. Meteor. Soc.*, **84 (8)**, 1063–1075.

Lorsolo, S. and A. Aksoy, 2012: Wavenumber analysis of azimuthally distributed data: Assessing maximum allowable gap size. *Mon. Wea. Rev.*, **140**, 1945–1956, doi: 10.1175/MWR-D-11-00219.1.

Louppe, G., 2014: Understanding random forests: from theory to practice. Ph.D. thesis, University of Líege.

Martinez, J., M. M. Bell, R. Rogers, and J. D. Doyle, 2019: Axisymmetric potential vorticity evolution of hurricane patricia (2015). *J. Atmos. Sci.*, **76**, 2043–2063, doi: 10.1175/JAS-D-18-0373.1.

McGovern, A., R. Lagerquist, D. J. Gagne, G. E. Jergensen, K. L. Elmore, C. R. Homeyer, and T. Smith, 2019: Making the black box more transparent: Understanding the physical implications of machine learning. *Bull. Amer. Meteor. Soc.*, **100 (11)**, 2175–2199.

Montgomery, M. T., 2016: Introduction to hurricnae dynamics: Tropical cyclone intensification. *Advanced Numerical Modeling and Data Assimilation Techniques for Tropical Cyclone Prediction*, U. C. Mohanty and S. G. Gopalakrishnan, Eds., Springer, Dordecht., chap. 21-22, "537–559".

Montgomery, M. T., M. E. Nicholls, T. A. Cram, and A. B. Saunders, 2006: A vortical hot tower route to tropical cyclogenesis. *J. Atmos. Sci.*, **63**, 355–386, doi: 10.1175/JAS3604.1.

Nolan, D. S., Y. Moon, and D. P. Stern, 2007: Tropical cyclone intensification from asymmetric convection: Energetics and efficiency. *J. Atmos. Sci.*, **64**, 3377–3405, doi: 10.1175/JAS3988.1.

NWS, 2019: Hurricane michael hits georgia. NOAA National Weather Service, cited: 2020-08-11, [Available online at `https://www.weather.gov/ffc/2018_hurricane_michael`].

Ooyama, K. V., 1969: Numerical simulation of the life cycle of tropical cyclones. *J. Atmos. Sci.*, **26**, 3–40, doi: 10.1175/1520-0469(1969)026<0003:NSOTLC>2.0.CO;2.

Ooyama, K. V., 1982: Numerical simulation of the life cycle of tropical cyclones. *J. Meteor. Soc. Japan*, **60**, 369–380, doi: 10.2151/jmsj1965.60.1_369.

Oye, R., C. Mueller, and S. Smith, 1995: Software for radar translation, visualization, editing, and interpolation. *Preprints of 27th Conf. on Radar Meteorology, Vail, CO, Amer. Meteor. Soc., 1995*, 359–361.

Pedregosa, F., et al., 2011: Scikit-learn: Machine learning in python. *Journal of Machine Learning Research*, **12**, 2825–2830.

Reasor, P. D., M. D. Eastin, and J. F. Gamache, 2009: Rapidly intensifying hurricane guillermo (1997). part i: Low-wavenumber structure and evolution. *Mon. Wea. Rev.*, **137**, 603–631, doi: 10.1175/2008MWR2487.1.

Rogers, R., 2010: Convective-scale structure and evolution during a high-resolution simulation of tropical cyclone rapid intensification. *J. Atmos. Sci.*, **67**, 44–70, doi: 10.1175/2009JAS3122.1.

Rogers, R., P. Reasor, and S. Lorsolo, 2013: Airborne doppler observations of the inner-core structural differences between intensifying and steady-state tropical cyclones. *Mon. Wea. Rev.*, **141**, 2970–2991, doi: 10.1175/MWR-D-12-00357.1.

Rogers, R. F., et al., 2017: Rewriting the tropical record books: The extraordinary intensification of hurricane patricia (2015). *Bull. Amer. Meteor. Soc.*, **98**, 2091–2112, doi: 10.1175/BAMS-D-16-0039.1.

Schubert, W. H. and J. J. Hack, 1983: Transformed eliassen balanced vortex model. *J. Atmos. Sci.*, **40**, 1571–1583, doi: 10.1175/1520-0469(1983)040<1571:TEBVM>2.0.CO;2.

Smith, R. K., 2006: Accurate determination of a balanced axisymmetric vortex in a compressible atmosphere. *Tellus*, **58**, 98–103, doi: 10.1111/j.1600-0870.2006.00149.x.

Stern, D. P. and D. S. Nolan, 2009: Reexamining the vertical structure of tangential winds in tropical cyclones: Observations and theory. *J. Atmos. Sci.*, **66**, 3579–3600, doi: 10.1175/2009JAS2916.1.

Stern, D. P. and D. S. Nolan, 2012: On the height of the warm core in tropical cyclones. *J. Atmos. Sci.*, **69**, 1657–1680, doi: 10.1175/JAS-D-11-010.1.

Stern, D. P. and F. Zhang, 2010: The warm-core structure of hurricane earl (2010). *J. Atmos. Sci.*, **73**, 3305–3328, doi: 10.1175/JAS-D-15-0328.1.

Testud, J., P. H. Hildebrand, and W.-C. Lee, 1995: A procedure to correct airborne doppler radar data for navigation errors using the echo returned from the earth's surface. *J. Atmos. Oceanic Technol.*, **12 (4)**, 800–820.

Trabing, B. C. and M. M. Bell, 2020: Understanding error distributions of hurricane intensity forecasts during rapid intensity changes. *Wea. Forecasting*, 1–43, doi: 10.1175/WAF-D-19-0253.1, URL `https://doi.org/10.1175/WAF-D-19-0253.1`, `https://journals.ametsoc.org/waf/article-pdf/doi/10.1175/WAF-D-19-0253.1/4996646/wafd190253.pdf`.

Van Sang, N., R. K. Smith, and M. T. Montgomery, 2008: Tropical-cyclone intensification and predictability in three dimensions. *Quart. J. Roy. Meteor. Soc.*, **137**, 563–582, doi: 10.1002/qj.235.

Vigh, J. A. and W. H. Schubert, 2009: Rapid development of the tropical cyclone warm core. *J. Atmos. Sci.*, **66**, 3335–3350, doi: 10.1175/2009JAS3092.1.

Wakimoto, R. M. and C. Liu, 1996: The garden city, kansas, storm during vortex 95. part ii: The wall cloud and tornado. *Mon. Wea. Rev.*, **126 (2)**, 393–408.

Wakimoto, R. M., H. V. Murthey, A. Nester, D. P. Jorgensen, and N. T. Atkins, 2006: High winds generated by bow echoes. part i: Overview of the omaha bow echo 5 july 2003 storm during bamex. *Mon. Wea. Rev.*, **134 (10)**, 2793–2812.

Weinkle, J., C. Landsea, D. Collins, R. Musulin, R. P. Crompton, P. J. Klotzbach, and R. Pielke Jr, 2018: Normalized hurricane damage in the continental united states 1900-2017. *Nat Sustain*, **1**, 808–813, doi: 10.1038/s41893-018-0165-2.

Willoughby, H. E., 1998: Tropical cyclone eye thermodynamics. *Mon. Wea. Rev.*, **126**, 3053–3067, doi: 10.1175/1520-0493(1998)126<3053:TCET>2.0.CO;2.

Zhang, L., Z. Pu, W.-C. Lee, and Q. Zhao, 2012: Thermodynamic retrieval in rapidly rotating vortices from multiple-doppler radar data. *Wea. Forecasting*, **27 (1)**, 231–239, doi: 10.1175/WAF-D-11-00028.1.